Perturbed Angular Correlation Spectroscopy –
A Tool for the Study of Defects and Diffusion at the Atomic Scale

Matthew Zacate[1,a] and Herbert Jaeger[2,b]

[1]Northern Kentucky University, Highland Heights, KY 41099, USA
[2]Miami University, Oxford, OH 45056, USA

[a]zacatem1@nku.edu, [b]jaegerh@muohio.edu

Abstract. This paper provides an introduction to perturbed angular correlation (PAC) spectroscopy in the context of its application in the study of point defects and diffusion. It emphasizes what we anticipate to be of interest to non-PAC specialists who are interested in understanding variations in how PAC results are presented by different research groups and in how physical quantities such as defect formation energies, association energies, and migration barriers can be extracted from analysis of PAC spectra. Numerous citations are included to emphasize the universality of the analysis methods across different classes of materials including metallic, ceramic, and semiconducting compounds.

Introduction

Perturbed angular correlation spectroscopy (PAC) has its origins in the field of nuclear physics; however, it has since had widespread application in solid state systems as described in a number of past review articles [1—16]. The most common application of PAC in the study of materials involves the time differential angular correlation between pairs of gamma rays emitted by radioactive nuclei, which serve as probes of the local electric charge distributions and magnetic fields in a material. Often the abbreviation TDPAC is used to emphasize that the method is time-differential PAC as opposed to time integrated PAC; however, IPAC is seldom used and PAC will be used in this paper to be synonymous with TDPAC. In a PAC experiment, the angular correlation between gamma rays changes in time in response to the hyperfine interaction (HFI) between the PAC probe nuclei and the electromagnetic environments of the material where the probes are located.

The present paper provides a detailed introduction to PAC with an emphasis on how physical quantities of interest to studies of defects and diffusion can be obtained. We have three goals in this paper: (1) to bridge introductory [3, 17] and comprehensive [18, 19] descriptions of PAC with an aim to help non-specialists understand variations in experimental setups and data analysis; (2) to provide an extended description of how adjustable parameters in fits of PAC spectra can be used in studies of defects and diffusion; and (3) to give a sense of the general applicability of PAC to all classes of materials by describing briefly and providing citations to studies in ceramic, semiconducting, and metallic compounds. Examples have been selected based primarily on their suitability for illustrating the analysis techniques discussed in this paper rather than on their impact in the understanding of defect and diffusion processes. As such, many important studies have not been included in this review, and the reader is encouraged to investigate other published works of the cited authors.
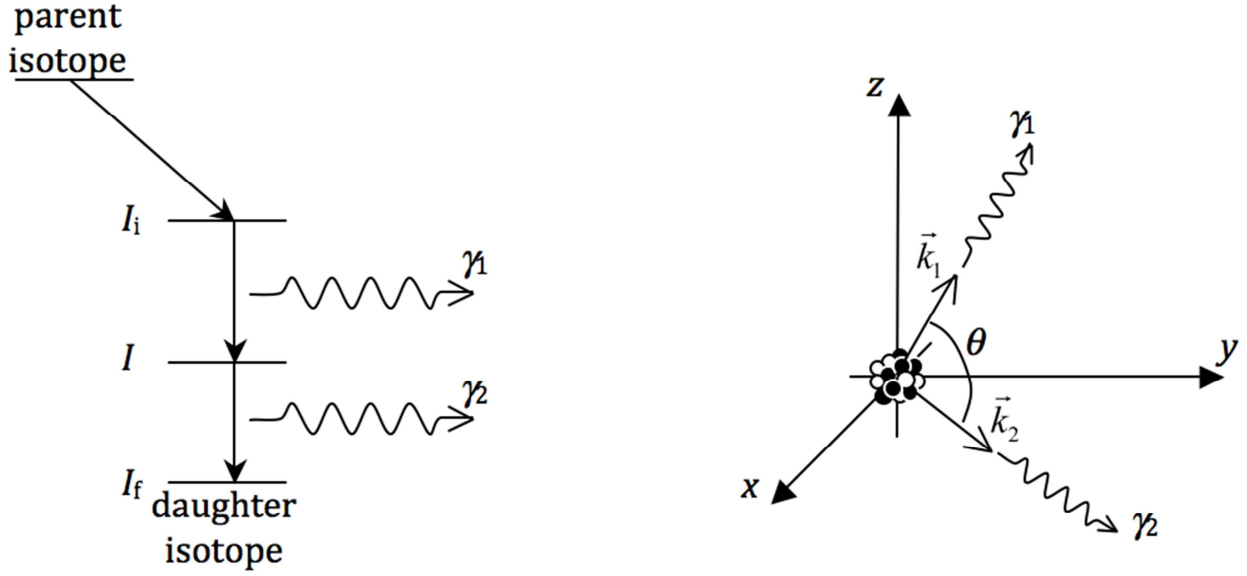
Fig. 1. A two-gamma nuclear cascade.

The paper is organized as follows. The first part provides an introduction to the theoretical underpinnings of PAC. The mathematical formalism used may be unfamiliar to some, so explanatory text is included to emphasize key results. A complete understanding of the derivation is not necessary to follow the rest of the paper, which consists of a section describing the most common spectrometer configurations and other experimental considerations and a section of example applications of PAC. This paper emphasizes the physical origins of and use of the quadrupole interaction (QI), one of the two basic HFIs that can be used to study defects. A companion paper by Carbonari, Mestnik-Filho, and Saxena [20] provides comparable information for the other basic HFI: the magnetic interaction (MI).

Theoretical Background

Angular correlation of a $\gamma - \gamma$ cascade. Consider a 3-level nucleus as show in Fig. 1. The excited state I_i decays by emission of γ_1 to the intermediate state I, followed by decay to the ground state I_f by emission of γ_2. The angular correlation function $W(\gamma_1, \gamma_2)$ is a measure of the probability that γ_1 is detected in direction $\vec{k}_1$ and γ_2 is detected in direction $\vec{k}_2$. Utilizing the density matrix formalism one finds [17, 18, 19]

$$W(\gamma_1, \gamma_2) = \sum_{mm'} \langle m | \rho(\gamma_2, 0) | m' \rangle \langle m' | \rho(\gamma_1, 0) | m \rangle. \tag{1}$$

$$\langle m' | \rho(\gamma_1, 0) | m \rangle = \sum_{k_1 N_1} (-1)^{2I - I_i + m} (2k_1 + 1)^{1/2} A_{k_1}(\gamma_1) \begin{pmatrix} I & I & k_1 \\ m' & -m & N_1 \end{pmatrix} D_{N_1 0}^{k_1}(z \to \gamma_1)$$

$$\tag{2}$$

$$\langle m | \rho(\gamma_2, 0) | m' \rangle = \sum_{k_2 N_2} (-1)^{k_2 - I_f - m} (2k_2 + 1)^{1/2} A_{k_2}(\gamma_2) \begin{pmatrix} I & I & k_2 \\ m' & -m & N_2 \end{pmatrix} D_{N_2 0}^{k_2 *}(\gamma_2 \to z).$$

Here $\rho(\gamma_i, 0)$ describes the state of the system immediately after the γ_1 emission (*i.e.* at $t = 0$). The matrix elements $\langle m | \rho(\gamma_i, 0) | m \rangle$ are the probabilities of finding the system in an eigenstate $| m \rangle$ immediately after the ith transition (Fig. 2). The explicit forms of these matrix elements are
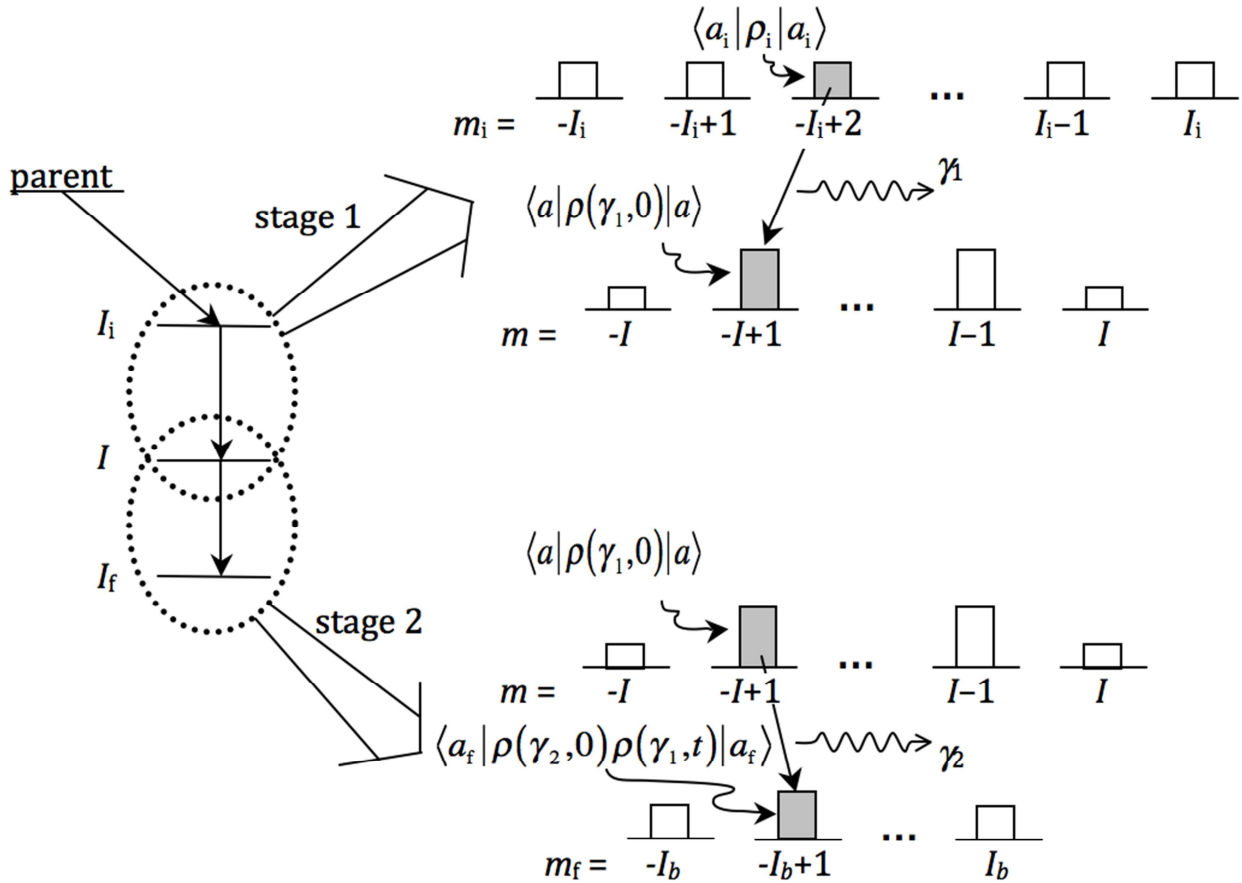
Fig. 2. Schematic representation of the two stages in an angular correlation measurement: (1) emission of a first γ – ray followed by (2) emission of the second γ – ray. Bars over magnetic substates represent their populations, which are unequal following the first γ – decay because of mutlipole radiation selection rules.

The $A_{k_i}(\gamma_i)$ are radiation parameters that depend on the spins of the levels involved in the transition and on the multipolarity of the radiation. The radiation parameters are normalized to $A_0 = 1$. The $D^{k_i}_{N_i 0}(\gamma_i \to z)$ are rotation matrices that transform the z-axis into the detection direction of γ_i. The $D^{k_i}_{N_i 0}$ can be expressed in terms of spherical harmonics $Y_{N_i 0}(\theta_i, \phi_i)$.

    Inserting (2) into (1) and performing the mm'–sum collapses the k_i and N_i sums into $k_1 = k_2 = k$ and $N_1 = N_2 = N$. The angular correlation function becomes

$$W(\gamma_1, \gamma_2) = \sum_{k \, N} (-1)^k A_k(\gamma_1) A_k(\gamma_2) \frac{Y^*_{kN}(\theta_1, \phi_1) Y_{kN}(\theta_2, \phi_2)}{(2k+1)}. \tag{3}$$

Summation over N reduces the spherical harmonics to Legendre polynomials

$$W(\theta) = \sum_{k=even}^{k_{max}} A_k P_k(\cos\theta) \tag{4}$$

with θ the angle between the detection directions of γ_1 and γ_2 and $A_k \equiv A_k(\gamma_1)A_k(\gamma_2)$. The sum is only over even k because the odd A_k vanish as a consequence of parity conservation and the fact that polarization of the γ photons is not measured. The summation is finite due to conservation of angular momentum. For the frequently used $I = \frac{5}{2}$ probe nuclei the summation index limit is $k_{max} = 4$, thus $W(\theta) = 1 + A_2 P_2(\cos\theta) + A_4 P_4(\cos\theta)$. The A_k are called the anisotropy factors.

    Angular correlation of a $\gamma - \gamma$ cascade with perturbations. Note that in Eq. 1 we have used the state of the system immediately after emission of γ_1. This is appropriate as long as there is no external field interacting with the nucleus. If we want to include interactions of the nucleus with extra-nuclear fields we must include the evolution of the density matrix from $t = 0$ to the time t just before emission of γ_2 (Fig. 3). Thus we replace $\rho(\gamma_1, 0)$ with $\rho(\gamma_1, t)$, which describes the state of the system a time t after emission of γ_1 immediately before emission of γ_2. The angular correlation function (1) now is written

$$W(\gamma_1, \gamma_2, t) = \sum_{mm'} \langle m | \rho(\gamma_2, 0) | m' \rangle \langle m' | \rho(\gamma_1, t) | m \rangle, \tag{5}$$

and the time dependence is expressed using an evolution operator $\Lambda(t)$, which transforms the density operator $\rho(\gamma_1, 0)$ into $\rho(\gamma_1, t)$:

$$\langle b | \rho(\gamma_1, t) | b' \rangle = \sum_{aa'} \langle b | \Lambda(t) | a \rangle \langle a | \rho(\gamma_1, 0) | a' \rangle \langle a' | \Lambda(t) | b' \rangle. \tag{6}$$

Inserting (6) into (5) and using (2), the angular correlation function becomes

$$W(\gamma_1, \gamma_2, t) = \sum_{k_1 k_2 N_1 N_2} A_{k_1}(\gamma_1) A_{k_2}(\gamma_2) G_{k_1 k_2}^{N_1 N_2}(t) \frac{Y_{k_1 N_1}^*(\theta_1, \phi_1) Y_{k_2 N_2}(\theta_2, \phi_2)}{\sqrt{(2k_1 + 1)(2k_2 + 1)}}. \tag{7}$$

The angles θ_i and ϕ_i refer to the detection direction of γ_1 with respect to the z-axis. $G_{k_1 k_2}^{N_1 N_2}(t)$ is the so-called perturbation factor which contains all time dependence and effects of the perturbation due to the interaction of the nucleus with external electric or magnetic fields. The perturbation factor is given by

$$G_{k_1 k_2}^{N_1 N_2}(t) = \sum_{aa'bb'} (-1)^{2I+a+b} \sqrt{(2k_1 + 1)(2k_2 + 1)} \times$$
$$\times \begin{pmatrix} I & I & k_1 \\ a' & -a & N_1 \end{pmatrix} \begin{pmatrix} I & I & k_2 \\ b' & -b & N_2 \end{pmatrix} \langle b | \Lambda(t) | a \rangle \langle b' | \Lambda(t) | a' \rangle^*. \tag{8}$$

The matrix elements of the evolution operator that appear in (8) can be expressed in terms of the evolution operator's eigenvalues and eigenvectors. For time-independent Hamiltonians, the eigenvalues are equal to $\exp(-iE_j t / \hbar)$ where E_j are the energies of the stationary nuclear spin states in the hyperfine interaction. It can be shown that (8) can be expressed as a sum of cosines:

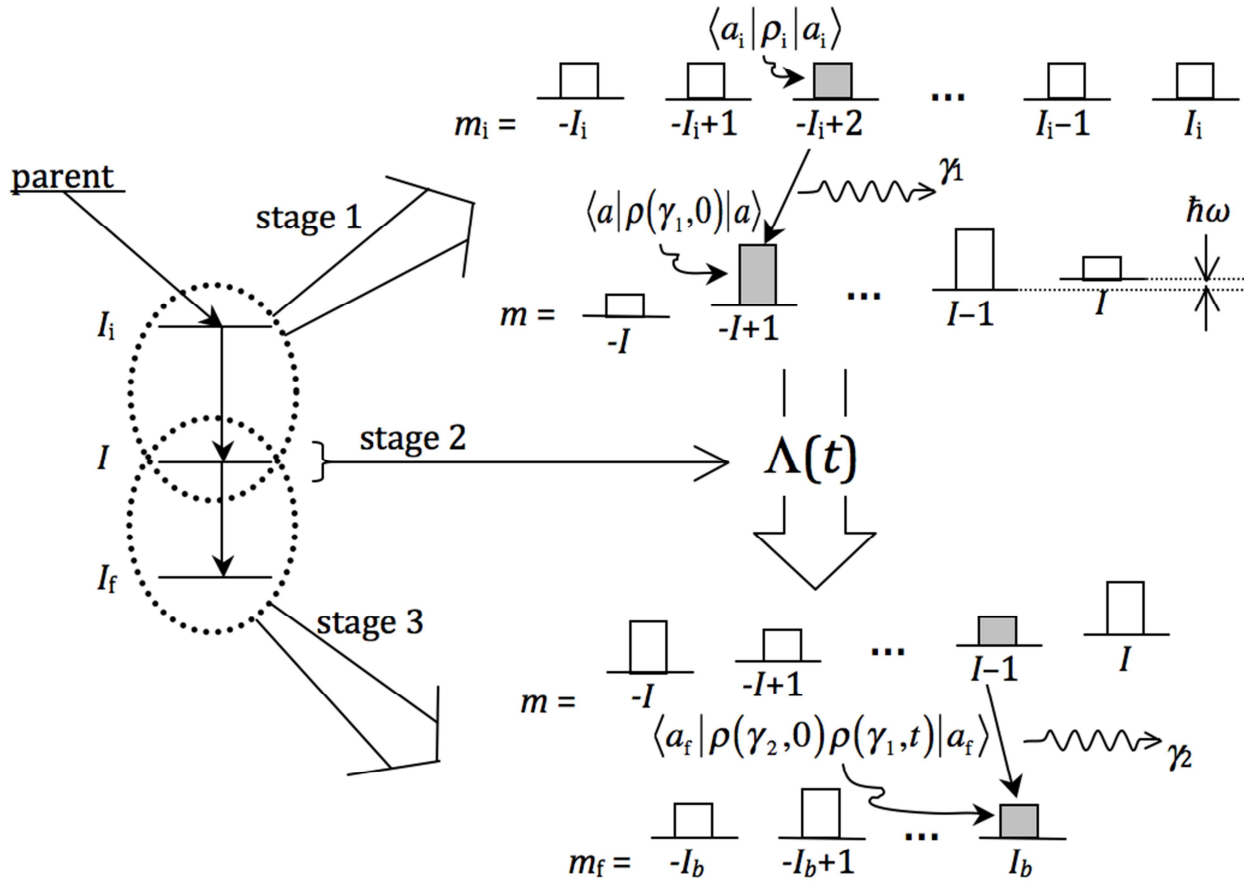$$G_{k_1 k_2}^{N_1 N_2}(t) = \sum_n S_{k_1 k_2, n}^{N_1 N_2} \cos(\omega_n t) \tag{9}$$

Fig. 3. The three stages of a perturbed angular correlation measurement: (1) emission of the first γ – ray, (2) evolution of the intermediate nuclear state of the daughter nucleus, and (3) emission of the second γ – ray. Bars over magnetic substates represent their populations, which evolve as determined by the evolution operator $\Lambda(t)$.

The angular frequencies ω_n in Eq. 9 come from differences in eigenvalues and therefore depend in general on the strengths and the symmetries of the hyperfine interactions. The amplitudes $S_{k_1 k_2, n}^{N_1 N_2}$ depend on the projections of eigenvectors along the nuclear spin basis vectors, and these depend in general on the value of the nuclear spin state, symmetry of the hyperfine interaction, and orientation of hyperfine symmetry axes with respect to directions of γ -ray detection.

A common experimental condition is to perform PAC measurements on polycrystalline samples. In such cases, one must average over all orientations of the symmetry axes of hyperfine interactions with respect to the directions of γ -ray detection in (7). The result is an angular correlation function that depends only on the angle between γ detections, θ, and time between detections, t:

$$W(\theta,t)=\sum_{\substack{k=0 \\ \text{even}}}^{k_{max}} A_{kk} G_{kk}(t) P_k(\cos\theta),\tag{10}$$

in which $G_{kk}(t)$ is the sum over all terms $G_{k_1 k_2}^{N_1 N_2}(t)$ with $k_1 = k_2 = k$. This can be written as a sum of cosines with a different set of amplitudes:

$$G_{kk}(t) = s_{k0} + \sum_n s_{kn} \cos(\omega_n t). \tag{11}$$

This new set of amplitudes does not depend on orientations of hyperfine interactions relative to detector directions.

Magnetic Dipole Interaction. The lowest order magnetic interaction is the magnetic dipole interaction (MI). It takes place between the magnetic dipole moment of a PAC probe and an extranuclear magnetic field. The dipole moment is proportional to the total angular momentum of the nucleus and is conventionally expressed in terms of the dimensionless g-factor. The magnetic field may be present in the form of a field applied from outside a sample or, in the case of ferromagnetic and antiferromagnetic materials, from spontaneous magnetic moments within the sample. In general, the magnetic field at the PAC probe nucleus is different from the external field because of spin polarization of the s electrons near the nuclear probe. Thus, different PAC probes will experience different magnetic interactions even when placed in the same extranuclear field.

Classically, a magnetic field exerts a torque on any nucleus with nonzero magnetic dipole moment, resulting in a precession of the moment about the field as illustrated in Fig. 4a. The frequency of precession is known as the Larmor frequency and is given by $\omega_L = -g(\mu_N / \hbar)B_0$, where g is the dimensionless g-factor, μ_N is the nuclear magneton, and B_0 is the magnitude of the magnetic field at the probe, *i.e.* the hyperfine magnetic field.

Quantum mechanically, the magnetic interaction results in a complete lifting of the degeneracy in the intermediate nuclear spin state of the PAC probe (Fig. 4b). The energy difference between successive m-states is $\hbar\omega_L$, leading to oscillations in populations of m-states with frequencies that are integer multiples of ω_L. The amplitudes in (9) depend on the experimental setup; in some cases, experimental configurations can be chosen so that the observed perturbation function $\vec{\tau}$ depends only on ω_L or on $2\omega_L$, as described in detail by Butz [21].
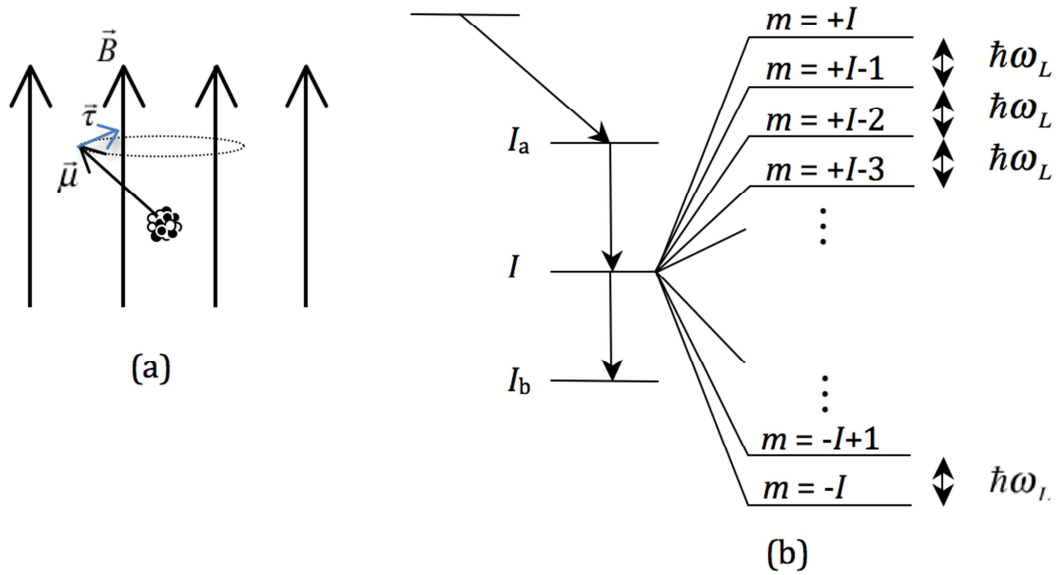

Fig. 4. Magnetic hyperfine interaction: (a) classical picture; (b) quantum mechanical picture.

Electric Quadrupole Interaction. The lowest order electric interaction is the quadrupole interaction (QI). It takes effect between the electric quadrupole moment of a PAC probe and the electric field gradient (EFG) arising from charges in the crystal surrounding the probe nucleus. The nuclear quadrupole moment Q is a single value that indicates how much the distribution of charge in the nucleus deviates from spherical. The EFG is a traceless, second-order tensor that is essentially the second spatial derivative of the electrostatic potential due to extranuclear charges. The tensor is reported customarily in terms of the principal component with largest magnitude, V_{zz}, and an asymmetry parameter η, defined by $\eta = \left(V_{xx} - V_{yy}\right)/V_{zz}$, where V_{xx} and V_{yy} are the other two principal components of the EFG tensor with the convention that $\left|V_{zz}\right| \geq \left|V_{yy}\right| \geq \left|V_{xx}\right|$.

The electric quadrupole interaction partially lifts the degeneracy in the intermediate nuclear spin state of the PAC probe (Fig. 5). The strength of the interaction is often reported in terms of the quadrupole interaction frequency $\omega_Q \equiv eQV_{zz}/\left[4I(2I-1)\hbar\right]$ where e is the fundamental unit of charge and I is the total spin of the intermediate nuclear state. An alternative and common way to report the strength of the interaction is by the quadrupole coupling frequency $\nu_Q \equiv eQV_{zz}/h$.

The frequencies that are present in the measured perturbation function (Eq. 9) are proportional to ω_Q. The number of frequencies that can be observed and the factors multiplying ω_Q depend in detail on the experimental setup, including orientation of EFG with respect to detectors in the case of single crystals, value of the intermediate nuclear spin I, and asymmetry of the EFG. As in the magnetic case, the amplitudes in the perturbation function depend on the experimental configuration. In addition, they depend on the spin of the probe and on the symmetry of the EFG.

For the important case of $I = 5/2$ probes, there are three observable frequencies ω_1, ω_2, and ω_3. When $\eta = 0$, the frequencies are given by $\omega_1 = 6\omega_Q$, $\omega_2 = 12\omega_Q$ and $\omega_3 = 18\omega_Q$ and the amplitudes are given by $s_0 = 1/5$, $s_1 = 13/35$, $s_2 = 2/7$, and $s_3 = 1/7$. More generally, the frequencies are functions of η: $\omega_1 = 2\sqrt{3}\alpha\omega_Q \sin\left(\frac{1}{3}\cos^{-1}\beta\right)$, $\omega_2 = 2\sqrt{3}\alpha\omega_Q \sin\left(\frac{\pi}{3} - \frac{1}{3}\cos^{-1}\beta\right)$, and $\omega_3 = 2\sqrt{3}\alpha\omega_Q \sin\left(\frac{\pi}{3} + \frac{1}{3}\cos^{-1}\beta\right)$ with $\alpha \equiv \sqrt{28\left(1 + \eta^2/3\right)}$ and $\beta \equiv 80\left(1 - \eta^2\right)/\alpha^3$, and the amplitudes have a complicated, but known, dependence on η (see references 22 and 23 for details). For amplitude- and η-dependencies of frequencies for non-5/2 spin probes, the reader is referred to the work of Butz [21].
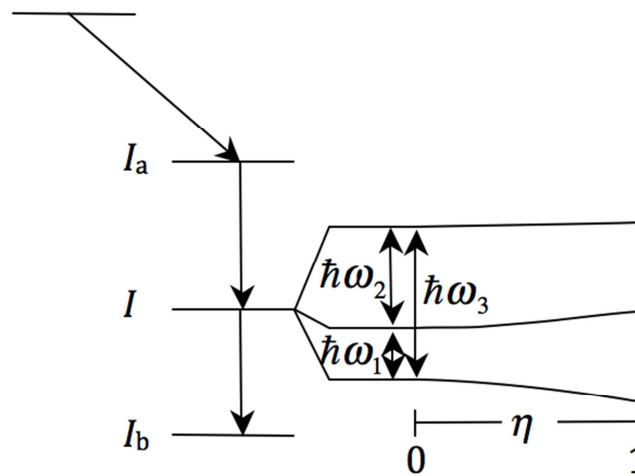

Fig. 5. Electric hyperfine interaction for I=5/2 PAC probes.

Mixed Electric and Magnetic Interaction. It is worth pointing out that it is possible to have a mixed magnetic and electric hyperfine interaction. Again, the frequencies that will be observable in the perturbation function are proportional to differences in energies of eigenstates of the HFI Hamiltonian. Unlike in the case of the pure magnetic interaction, the energy spacing will not be regular, and in general there will be a sizable number of frequencies. It is outside the scope of the present paper to go further into the case of mixed interactions except to assert that it is possible to calculate such perturbation functions theoretically and analyze experimental spectra containing signals that originate from mixed interactions. See, for example, references 24 and 25.

Hyperfine Interactions in Materials. The atomic displacements near PAC probes that occur because of lattice vibrations result in fluctuations in the MI and the QI experienced by the PAC probes. The timescale of a hyperfine measurement is defined by the reciprocal of the hyperfine interaction frequency: $1/\omega_L$ in the case of the MI and $1/\omega_Q$ in the case of the QI. Lattice vibration frequencies typically are several orders of magnitude larger than hyperfine interaction frequencies, and as a consequence, measurements are not sensitive to the variations in HFI induced by the lattice vibrations. Instead, the measurement can be considered to be of a static HFI, the magnetic field or EFG being the time-average over many lattice vibrations. So, when discussing HFIs in a solid, one usually speaks in terms of "static" HFIs. Exceptions to this include situations where point defects near probes jump from one lattice site to another, when the probes themselves jump, or when there are fluctuations in the charge state of defect-probe complexes at a timescale comparable to the HFI frequency, and these are considered separately below as "dynamic" hyperfine interactions.

PAC probes in materials can experience a range of crystallographic environments, depending on the site occupation of the probes, or where the probes substitute in the material, and these environments in turn can be disturbed by defects. For dilute defect concentrations and when defects are attracted to PAC probes, a distinct set of HFIs arise in addition to the defect-free HFIs. For non-dilute defect concentrations and little attraction to PAC probes, the defect-free or lattice HFIs are disturbed slightly, resulting in a distribution of HFIs, the central, or most probable of which, is near the lattice HFI. For non-dilute concentrations and strong attraction, a combination of these effects is observed.

It remains to consider the physical origins of HFIs in materials. The accompanying review article by Carbonari, Mestnik-Filho, and Saxena [20] provides a thorough introduction to the magnetic interaction. The remainder of the present section examines the physical origin of the electric field gradient, which is responsible for the quadrupole interaction.

The EFG at a nucleus is given by

$$V_{ij} = \int \frac{1}{r^5} \left(3x_i x_j - r^2 \delta_{ij} \right) \rho\left(\vec{r}\right) d\tau , \qquad (12)$$

where $\rho\left(\vec{r}\right)$ is the charge density of everything except the nucleus-of-interest and consists of the electrons of the remaining solid, including the ion-core electrons of the atom that contains the nucleus of interest, and the positive charges of the other nuclei. The EFG has the same symmetry as the point symmetry at the location of the nucleus through its dependence on $\rho\left(\vec{r}\right)$. The variation with $1/r^3$ means that the EFG is especially sensitive to non-spherical or non-cubic electronic density contributions near the nucleus of interest, especially those arising from unfilled valence orbitals and distortions of core electron orbitals.

For nuclei located at crystal lattice sites with cubic site symmetry, the EFG experienced by the nuclei is "zero;" that is, $V_{zz} = 0$. For sites with a threefold or higher axis of symmetry, $V_{zz} \neq 0$, $\eta = 0$, and the principal axis of the EFG is collinear with the axis of symmetry. For lower symmetry, $V_{zz} \neq 0$ and $0 \leq \eta \leq 1$. Arguably one of the most straightforward ways to detect point

defects using PAC occurs when it is possible to measure the EFG at probe nuclei without nearby defects and compare it to EFGs measured when defects are in first or second neighbor positions, especially when the change in local charge distribution induced by the point defects lowers the local symmetry.

As an example of detection of defects by reduction of symmetry, Fe vacancies in FeAl are considered. Al-lattice sites have $m\overline{3}m$ point symmetry, so that a PAC probe at an Al site experiences $V_{zz} = 0$ when no defects are nearby (Fig. 6a). A single vacancy in a near neighbor Fe site results in an axially symmetric EFG ($V_{zz} \neq 0$ and $\eta = 0$) with principal axis oriented in the direction of the neighboring Fe vacancy (Fig. 6b). A second vacancy in a near neighbor site adjacent to the first vacancy further reduces the local symmetry and a non-axially EFG is observed (Fig. 6c). Other arrangements of vacancies around probes lead to still more distinguishable EFGs [26].

One can determine the atomic structure near a probe based on the EFG the probe experiences – in principle. That is, when there are no defects in the probe's local environment, one could determine the lattice site the probe occupies by the EFG, as long as the sites have unique EFGs. An example for which this does not work is a structure such as the CsCl-structure, as both Cs and Cl sites have $m\overline{3}m$ point symmetry so that $V_{zz} = 0$. But even in such a case, if defects are in the probe's local environment, then one expects to be able to determine which types of defects are there and how they are arranged based on observed EFGs.

In some cases, consideration of symmetry alone is not sufficient to identify site occupation or defect configurations. Examination of how observed signals change when varying experimental configurations such as sample composition or measurement temperature can help identify the origins of observed QIs. Such arguments often are used in conjunction with estimates of strengths of QIs based on calculations of EFGs using simple point charge approximations. Here, we use the term point charge approximation generically to refer to any scheme that models the atoms or ions in a solid as point charges, including application of empirical corrections to account for distortions of the PAC probe's atomic orbitals derived either from theoretical calculations such as in references 27 and 28 or deduced from experimental trends such as in references 29 and 30. However, point charge approximations are not always sufficient for identifying origins of QIs, and more rigorous calculations of EFGs within the framework of density functional theory (DFT) must be performed.

Unfortunately, it is not always practicable or even possible to identify the origin of an observed EFG based on predictions from DFT calculations. For reliable prediction of EFGs in the presence of point defects, calculations must allow for relaxation of the crystal structure with atomic displacements also to be predicted in the DFT calculations. Most commonly, a supercell approach is used, in which the PAC probe is located at the center of a supercell that is large enough to accommodate significant relaxation but small enough to be computationally tractable. The sensitivity of EFGs to electronic densities of core electrons means that methods descended from the augmented plane wave approach must be employed rather than the widely used pseudopotential plane wave approach. Even then, calculated EFGs depend on the approximation chosen for the exchange and correlation terms in the energy, which lead to uncertainties in predicted values. In cases where differences among predicted EFGs for candidate crystallographic environments are greater than the uncertainties due to choice of exchange-correlation functional, comparison to experimentally measured values does allow one to determine site substitution and identify defect arrangements.

In general, measured QI frequencies vary with temperature, indicating of course that the corresponding EFGs vary with temperature. In non-cubic metals, the EFG decreases with increasing temperature; however, the degree of variation is too large to be due only to thermal expansion [31–33]. It was long suspected that the temperature dependence is linked to phonons, but it was not until only recently that the temperature dependence of the EFG in Cd metal was calculated from first principles to verify this picture [34]. It appears that temperature variations of EFGs in other materials systems can come from alternate sources. For example, calculations of the

EFG experienced by Ta dopants in TiO_2 indicate that the primary cause of temperature dependence comes from a structural relaxation around the dopant, the degree of which depends strongly on lattice parameter, which in turn varies due to thermal expansion [35]; thus, thermal expansion can contribute significantly to the temperature variation of EFGs, at least indirectly. A complete description of measured QI frequencies therefore must include information about their dependence on temperature. Such information is not always reported because it is not easily measured or is superfluous to the main focus of a particular study.

Perturbation functions when probes are in multiple environments. The perturbation functions given by Eqs. 9 and 11 assume all probes are in the same crystallographic environment. There are many interesting applications when probes are in more than one environment. In this case, Eqs. 7 and 10 can be written

$$W\left(\gamma_1,\gamma_2,t\right)= \sum_{k_1 k_2 N_1 N_2} A_{k1}\left(\gamma_1\right)A_{k2}\left(\gamma_2\right)\overline{G_{k_1 k_2}^{N_1 N_2}}\left(t\right)\frac{Y_{k_1 N_1}^*\left(\theta_1,\varphi_1\right)Y_{k_2 N_2}\left(\theta_2,\varphi_2\right)}{\sqrt{\left(2k_1+1\right)\left(2k_2+1\right)}},\tag{13}$$

and

$$W\left(\theta,t\right)=\sum_{\substack{k=0\\ even}}^{k_{max}} A_{kk}\overline{G_{kk}}\left(t\right)P_k\left(\cos\theta\right),\tag{14}$$

where the bar over the perturbation function indicates an average of the single-interaction perturbation functions of the individual environments. Three situations are described in more detail below: (1) probes are in a few discrete static environments, or sites, (2) probes are in an inhomogeneous environment that results effectively in a continuous distribution of static HFIs, and (3) probes experience fluctuating HFIs as the environment around a probe changes.
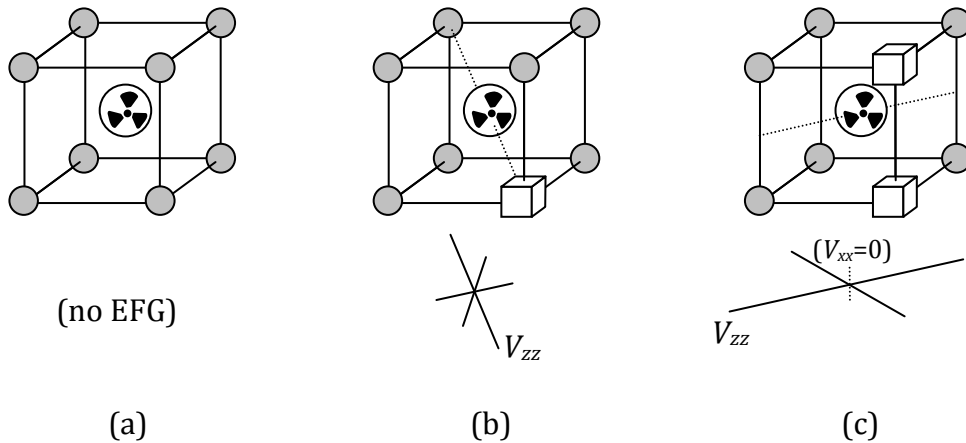

Fig. 6. Examples of defects causing EFGs at the location of the radioactive probe atom.

Discrete set of HFIs – site fractions. If there are N distinct hyperfine environments, then the average perturbation function is given as a weighted sum of the perturbation functions of the individual environments:

$$\overline{G_{kk}}(t) = \sum_{j=1}^{N} f_j G_{kk,j}(t), \tag{15}$$

where $G_{kk,j}(t)$ is the perturbation function that corresponds to the hyperfine interaction of the jth environment and f_j is the site fraction, or fraction of probes, in environment j. The f_j are normalized; that is, $\sum_{j=1}^{N} f_j = 1$.

Continuous distribution of HFIs. Sample inhomogeneity, due for instance to randomly distributed defects outside the first couple of near neighbor shells of the probes, results in a distribution of quadrupole interactions. This leads to a damping of the PAC signal. The effect is known as inhomogeneous broadening because it appears as a broadening of frequency distributions when viewing Fourier transforms of PAC spectra. The more defects there are in a system, the larger the disturbance to a HFI will be and the greater the inhomogeneous broadening.

There have been several theoretical studies done to clarify the physical sources of the broadening and to explore lineshapes for special cases [36–44]; however, a universal expression for lineshape that is appropriate for broadening caused by charged defects distributed randomly on a crystal lattice has not yet been established. The usual approach when analyzing PAC spectra is to assume that the distribution of EFGs leads to a Gaussian or Lorentzian distribution of frequencies. For example, this leads to

$$\overline{G_{kk}}(t) = s_{k0} + \sum_n s_{kn} \cos(\omega_n t) \exp\left[-\tfrac{1}{p}(\delta\omega_n t)^p\right], \tag{16}$$

for 5/2 spin probes in a polycrystalline sample. Here, p determines the type of distribution: 1 for Lorentzian and 2 for Gaussian. The full width half maximum (FWHM) of the Lorentzian distribution is given by 2δ, whereas the FWHM of the Gaussian distribution is $2\delta\sqrt{2\ln 2}$. Simulations of PAC spectra in the presence of randomly distributed defects have shown that there is an interdependence among empirical fitting parameters so that $\omega_n = \omega_n(\delta)$, or alternatively, $\omega_Q = \omega_Q(\delta)$ and $\eta = \eta(\delta)$ [45, 46].

There is some variation in how the width of the distribution is reported in the literature. Many authors use an exponential term of the form $\exp\left[-\tfrac{1}{p}(g_n\sigma t)^p\right]$ or $\exp\left[-\tfrac{1}{2}(g_n\sigma t)^p\right]$, where σ is an absolute measure of distribution width* and the g_n factors are proportional to the interaction frequencies ω_n. The relations $g_n = \omega_n/\nu_Q$, $g_n = \omega_n/\omega_Q$, and $g_n = \omega_n/\omega_1$ all have appeared in the literature.

---

*σ is not universally accepted as the symbol to use for absolute width and, for example, some authors use δ for absolute width.

Fluctuating HFIs. When fluctuations occur among multiple HFIs at a time scale comparable to $1/\omega_L$ or $1/\omega_Q$, the perturbation function can no longer be described simply by a superposition of static HFIs, as in Eq. 15. The method for modeling stochastic fluctuations of HFIs by Winkler and Gerdau [47] allows derivation of an appropriate expression for the angular correlation function by employing the Liouville formalism, so that Eq. 5 becomes

$$W(y_1, y_2, t) = \sum_{rbb'} \hat{\rho}(y_2, 0) | rbb')(rbb' | \hat{\rho}(y_1, t), \tag{17}$$

where r is an index that spans all possible HFIs, b and b' are sums over m-states of the intermediate nuclear state, and $\hat{\rho}(y_2, 0)$ and $\hat{\rho}(y_1, t)$ are vectors in the Liouville space, defined here by $|rmm') \equiv |r\rangle |m\rangle\langle m'|\langle r|$). The $\hat{\rho}(y_i, 0)$ are given by $(rbb' | \hat{\rho}(y_i, 0) = \text{prob}(r)\langle b | \rho(y_i, 0) | b'\rangle$, where $\langle b | \rho(y_i, 0) | b'\rangle$ is given by Eq. 2 and prob(r) denotes the probability of the system being found in state r at the instant of the y-ray emission.

For random fluctuations that are independent of history among static HFIs, the evolution operator can be expressed as $\hat{\Omega}(t) = \exp(\hat{B}t)$, where $\hat{B}$ is known as the Blume matrix [47]. The $\hat{B}$ is constructed from the Hamiltonians of all HFIs through which the system evolves and the rates of transition among the accessible HFIs as described in detail in refs. 47 and 48. The evolution operator matrix elements are written $(rbb' | \hat{\Omega}(t) | qaa')$ so that Eq. 6 becomes

$$(rbb' | \hat{\rho}(y_1, t) = \sum_{qaa'} p_{0,q} (rbb' | \hat{\Omega}(t) | qaa')\langle a | \rho(y_1, 0) | a'\rangle, \tag{18}$$

where $p_{0,q}$ is the probability that the system is in HFI state q at the time of the first gamma emission.

Within the Liouville formalism, Eq. 7 does not change and Eq. 8 becomes

$$G_{k_1 k_2}^{N_1 N_2}(t) = \sum_{aa'bb'} (-1)^{2I+a+b} \sqrt{(2k_1+1)(2k_2+1)} \begin{pmatrix} I & I & k_1 \\ a' & -a & N_1 \end{pmatrix} \begin{pmatrix} I & I & k_2 \\ b' & -a & N_2 \end{pmatrix} \times$$
$$\times \sum_{qr} p_{0,q} (rbb' | \hat{\Omega}(t) | qaa') \tag{19}$$

For most interesting physical cases, the evolution operator can be diagonalized so that the $(rbb' | \hat{\Omega}(t) | qaa')$ factor can be written $(rbb' | \hat{\Omega}(t) | qaa') = (rbb' | N_m)(M_m | qaa')\exp(-(\lambda_m - i\omega_m)t)$ where $(M_m |$ and $| N_m)$ are the mth left and right eigenvectors of the Blume matrix and $-\lambda_m + i\omega_m$ is the mth eigenvalue.

In the presence of fluctuating HFIs, an equation similar to Eq. 9 can be obtained:

$$G_{k_1 k_2}^{N_1 N_2}(t) = \sum_n S_{k_1 k_2, n}^{N_1 N_2} \exp(-\lambda_n t)\cos(\omega_n t) \tag{20}$$

where the ω_n come from the imaginary parts of the eigenvalues of the Blume matrix, the exponential decay constants λ_n come from the real parts of the eigenvalues, and the amplitude factors $S_{k_1 k_2, n}^{N_1 N_2}$ depend on projections of the eigenvectors of the Blume matrix along the state vectors

in Liouville space. The primary result of the fluctuating HFIs is that the perturbation function becomes damped through the presence of the exponential decay factors. A secondary effect is that the interaction frequencies can deviate from the frequencies that would be observed in a superposition of static HFIs; however, this deviation may or may not be as pronounced as the damping, depending on the underlying HFI fluctuation rates.

A rigorous calculation of the perturbation function can be made when the changes in HFIs are connected to changes in the physical origins of the HFIs within the stochastic model. In cases involving fluctuations among charge states, the HFI fluctuation rates in the stochastic model are simply the charge fluctuation rates. In cases involving atomic jumps of defects, changes in HFIs are connected to defect jump paths and jump rates. Measurement of the damping parameters λ_n then allows one to determine the charge fluctuation rates or atomic jump rates.

For fluctuations caused by atomic jumps, the accessible HFIs and rates of transition in the stochastic model of hyperfine interactions depend on crystal structure, defect concentrations, and atomic jump vectors. In general, stochastic models and their corresponding theoretical expressions for PAC perturbation functions must be considered in detail on a case-by-case basis. There have been several detailed investigations of how damping constants and frequencies depend on fluctuation rates [49, 50, 51] for a variety of models. The results of these investigations can be used to analyze experimental spectra obtained from physical situations that can be described by those models. Unfortunately, though, many physical situations examined in experiments are not included in those previous analyses, and alternate means of analyzing experimental data must be used.

Often, empirical expressions for fluctuating HFIs based on the results of Baudry and Boyer [52] and on Forker *et al.* [53] are used when analyzing PAC spectra. At least for "simple" fluctuation models, one can to a good approximation express the average perturbation function in two different fluctuation regimes: a slow fluctuation regime in which HFI fluctuation rates are less than ω_L or ω_Q and a fast fluctuation regime in which the rates are greater than ω_L or ω_Q. Then

$$\overline{G_{kk}}(t) = \begin{cases} \exp(-\lambda_{\text{slow}}t)G_{kk,\text{Static}}(t), & \text{slow regime} \\ \exp(-\lambda_{\text{fast}}t)G_{kk,\text{M.A.}}(t), & \text{fast regime} \end{cases} \tag{21}$$

provides a reasonable approximation in the two regimes. Here, $G_{kk,\text{Static}}(t)$ is the superposition of perturbation function that originates from probes distributed among the attainable static HFIs and $G_{kk,\text{M.A.}}(t)$ is the perturbation function that results from the average of attainable HFIs in the motionally averaged limit. The damping rate λ_{slow} is proportional to HFI fluctuation rate (and the underlying defect jump rate) and λ_{fast} is inversely proportional to fluctuation rate.

It is worth pointing out that for many fluctuating systems, the λ_n is nonzero even when ω_n is zero so that the non-oscillating contribution to the perturbation factor can be damped. This is in contrast to the case of inhomogenous broadening, for which zero frequency terms do not have an exponential damping factor. Thus, observation that the non-oscillating portion of a perturbation function decays to zero is evidence for dynamic effects.

Experimental Considerations

PAC Probes. The PAC probe nucleus acts as a foreign agent, a spy so-to-speak, that scopes out its environment and reports its observations in code by emitting correlated γ − ray pairs. To be suitable as a PAC probe a nucleus must decay from an excited state via emission of two γ − rays. The intermediate state must have a reasonably long lifetime so that the probe has time to "feel" the extra-nuclear fields and to interact with them. Ideally, the γ − ray energies are sufficiently different so that γ_1 and γ_2 can be distinguished. Moreover, the nuclear moments of the intermediate state, as well as the anisotropy of the angular correlation between γ − rays have to be large enough to

allow for measurement of the perturbation function. Last but not least the parent nucleus must be readily available or produced, and it must have a long enough lifetime to be practical to work with.

There are about 10-20 nuclei that can be used as PAC probes; however, in practice most of the PAC work reported in the literature is done with two probes: ^{111}Cd and ^{181}Ta. Table 1 lists some of the properties of these two nuclei, as well as those of ^{140}Ce and ^{44}Sc, two probes utilized by authors in this volume.

^{111}Cd is the decay product of electron-capture-decay of ^{111}In with a half-life of 2.83 days. The parent nuclei are produced in an accelerator either by ^{110}Cd (d,n)^{111}In or by alpha-bombardment of silver, ^{109}Ag(α, 2n)^{111}In. As ^{111}In is frequently used in biomedical and pharmaceutical research, it is readily available and usually comes dissolved in dilute aqueous HCl. Usually, ^{111}In-activity is either diffused into the material under study or implanted with a heavy-ion accelerator. Because of the relatively short parent half-life, an ^{111}In-sample retains adequate activity to be used for about two weeks.

^{181}Ta is the product of β$^-$ decay of ^{181}Hf which is easily prepared by irradiating natural Hf in a flux of thermal neutrons, ^{180}Hf(n, γ)^{181}Hf. Because of the large absorption cross section of ^{180}Hf for thermal neutrons, typical irradiation times are a few minutes to few hours. ^{181}Hf-samples retain sufficient activity to perform experiments for 3–4 months.

Most PAC probes, and all the ones in Table 1, have two distinct chemical identities: one determined by the parent nucleus and one by its daughter nucleus. Sometimes researchers identify the PAC isotope used according to its parent and sometimes by its daughter. To add to the confusion, different physical quantities are measured when the probe is in its parent form versus its daughter form. Equilibrium distributions of probe-defect complexes, which determine site fractions, are established by the parent state. In general, the time between transmutation to the emission of the first gamma ray is short enough that these complexes remain intact during the double–γ cascade, at least at room temperature. But, the time is long enough for the newly formed daughter and the atoms around it to have a chance to relax to the optimal configuration. Thus, interaction frequencies (and amplitudes in the case of non-polycrystalline samples) depend on the daughter state. Fluctuating HFIs are detected when their rates of change are comparable to the inverse lifetime of the intermediate state of the daughter probe, so dynamic effects are correctly expressed in terms of behavior associated with the daughter state of the probe.

PAC Spectrometer. Measurement of the (unperturbed) angular correlation of two γ – rays is usually performed with one fixed and one movable detector. The γ − γ coincidences are recorded for equal time intervals with varying angles between the detectors.

Hyperfine interactions between the PAC probe's moments and extra-nuclear fields result in a modulation of the coincidence count rate, in which case it is not necessary to measure count rate as a function of angle. Instead, a PAC spectrometer is configured with 3 or 4 detectors arranged in fixed angular intervals. The most common arrangement uses 4 detectors at 90˚ intervals, and

Table 1: Properties of PAC probe nuclei relevant for this volume. $T_{1/2}$ is the half-life of the parent nucleus, I and $t_{1/2}$ are nuclear spin and half-life of the intermediate level in the $γ_1 − γ_2$ cascade. g-factors and quadrupole moments are of the intermediate state

Parent to probe decay	A_2	$T_{1/2}$	$γ_1$ [keV]	$γ_2$ [keV]	I	$t_{1/2}$ [ns]	g-factor	Quadrupole Moment [b]
^{111}In→^{111}Cd	−0.18	2.83 d	171	245	5/2	85	−0.306	+0.83(13)
^{181}Hf→^{181}Ta	−0.288	42.4 d	137	482	5/2	10.8	+1.316	+2.35(6)
^{140}La→^{140}Ce	+0.04	1.68 d	329	487	4	3.5	+1.014	+0.35(7)
^{44}Ti→^{44}Sc	−0.092	49 y	78	65	1	156	+0.344	+0.214(3)

delayed coincidences between the 90° and 180° detector pairs are recorded and stored as histograms in a multichannel analyzer (MCA) or a computer acting as an MCA. Schematics of two common fixed detector spectrometer designs are shown in Fig. 7.

Most PAC spectrometers use scintillation detectors, such as BaF_2 or NaI mounted on photomultiplier tubes (PMT). These scintillator materials combine high detection efficiency with both reasonable energy and excellent time resolution. More recently Lutetium-Oxyorthosilicate (LSO) scintillators have been used successfully. LSO combines a time resolution almost as high as BaF2 with a greater detection probability and better light output [54]. Scintillators can be of cylindrical shape, 1-2" in height and diameter; however, to obtain the best solid-angle properties they are frequently in the shape of a truncated cone.

Detectors usually provide two output signals; the dynode, or "slow signal" is typically taken off the 7th to 10th dynode of the PMT, and its pulse height is proportional to the energy of the absorbed γ – ray. The anode signal, also referred to as the "fast signal", comes from the PMT's anode and provides a relatively precise indicator of the actual time of detection of the γ – ray. The dynode signal output is shaped by an on-board RC network and provides a signal with relatively good energy resolution.

Most PAC spectrometers in use today are based on the fast-slow coincidence method, which uses the fast signals for timing information and the slow signals for energy information. The timing information is derived from the fast signal by so-called constant fraction discrimination (CFD). Compared to simple leading edge triggering this provides superior timing properties as it eliminates amplitude-dependent walk for signals with variations in rise times. The slow signal is amplified and then sent to two energy discriminators*, which generate a logic pulse if the amplified slow signal falls into the energy window defined by a lower and upper discriminator level.

Of the fast-slow coincidence PAC spectrometers, there are two basic designs that are in use, labeled below and in Fig. 7 as type I and type II.

Type I Spectrometer. The logic signals from all energy discriminators associated with the various detectors are fed into the so-called routing logic, which provides a digital code indicating which γ was absorbed in which detector. The routing code is then used to address a specific storage area in the multichannel analyzer that is used to record the delayed coincidence events. Moreover, the routing logic also determines if a particular event is valid. A valid event means a γ_1 was detected in one detector followed by a γ_2 in another detector, while the other detectors did not register a γ_1 or γ_2.

Meanwhile all CFD outputs are logically ORed and connected to the start and stop inputs of a time-to-analog converter (TAC). The TAC functions as a clock and provides an analog output with a pulse height proportional to the time between the start and the stop signal. The TAC output is converted into a digital representation of the time difference in an analog-to-digital converter (ADC), which is connected to the multichannel analyzer and is gated by the routing logic. For valid events the ADC output is recorded in the appropriate memory bank of the MCA, while the routing logic inhibits the TAC for all invalid events. Note that in some spectrometers, the ADC and MCA are contained in a single module.

Type II Spectrometer. The energy discriminator output signal tuned to γ_1 for a specific detector is used to gate the CFD signal of the same detector. The gated CFD signals are then logically ORed to provide the start signal for the TAC. Similarly the CFD signal is gated by the energy discriminator output signal tuned to γ_2 and logically ORed to generate the stop signal for the TAC. In this way the TAC is started and stopped only by signals that satisfy the proper energy relationship, i.e. the TAC will not be started or stopped by a signal that does not correspond to a γ_1 or a γ_2 as is possible in a type I spectrometer. A routing logic similar to that used in a type I
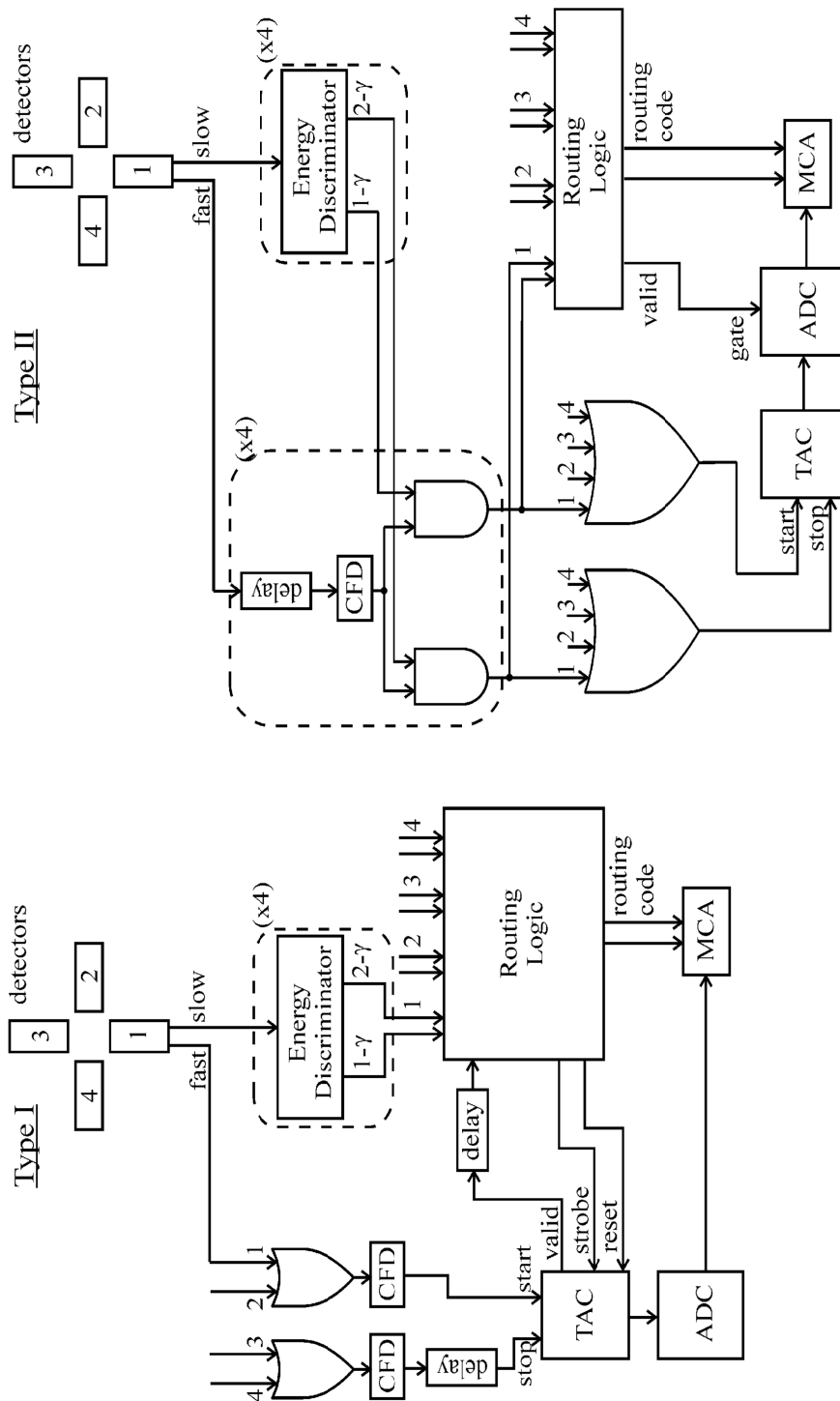
---

*Also known as Single Channel Analyzers.

Fig. 7. Block diagrams of two PAC spectrometer designs.

spectrometer is employed to determine which detector pair was involved with the event, so it can be stored in the appropriate memory bank of the MCA. A type II spectrometer performs a pre-selection of pulses before they are used to start and stop the TAC, while in type I valid as well as invalid events, or even γ – rays that are neither γ_1 nor γ_2, will start and stop the TAC. This limits the source activity that can be used with a type I spectrometer to lower values than can be used with a type II spectrometer. However, the type II spectrometer requires additional circuitry to accomplish this and thus is more complex. In particular a long delay of the CFD signals is required in order to gate them by the slower energy discriminator signals. The long delay is avoided in the type I spectrometer as the evaluation of the event validity goes on while the TAC processes the timing information. By the time the TAC is finished and makes available the output pulse, the slow signals have been processed by the routing logic and a decision can be made as to forward the timing signal to the MCA or discard it altogether.

There are alternatives to the fast-slow spectrometer design. One notable design is a fast-fast system that reduces the amount of nuclear instrumentation needed to construct a complete spectrometer [55]. Recently, there has been a trend to develop spectrometers that process outputs of the scintillation detectors digitally. Once the detector signals are digitized, further processing is done entirely in software, thus significantly reducing the amount of hardware needed [56, 57].

Data Reduction. The goal in a PAC experiment is to analyze the modulations in coincidence count rate stored in the multichannel analyzer as histograms for each pair of detectors. Figure 8 illustrates the process used to arrive at the PAC spectrum known as the counting rate ratio $R(t)$ from the raw counting rate data.

The number of counts that correspond to a time t between events in detectors i and j can be written $C_{ij}\left(\theta_{ij},t\right)= N_{ij}\left(\theta_{ij},t\right)+ B_{ij}\left(\theta_{ij},t\right)$, where θ_{ij} is the angle between detectors i and j, $N_{ij}\left(\theta_{ij},t\right)$
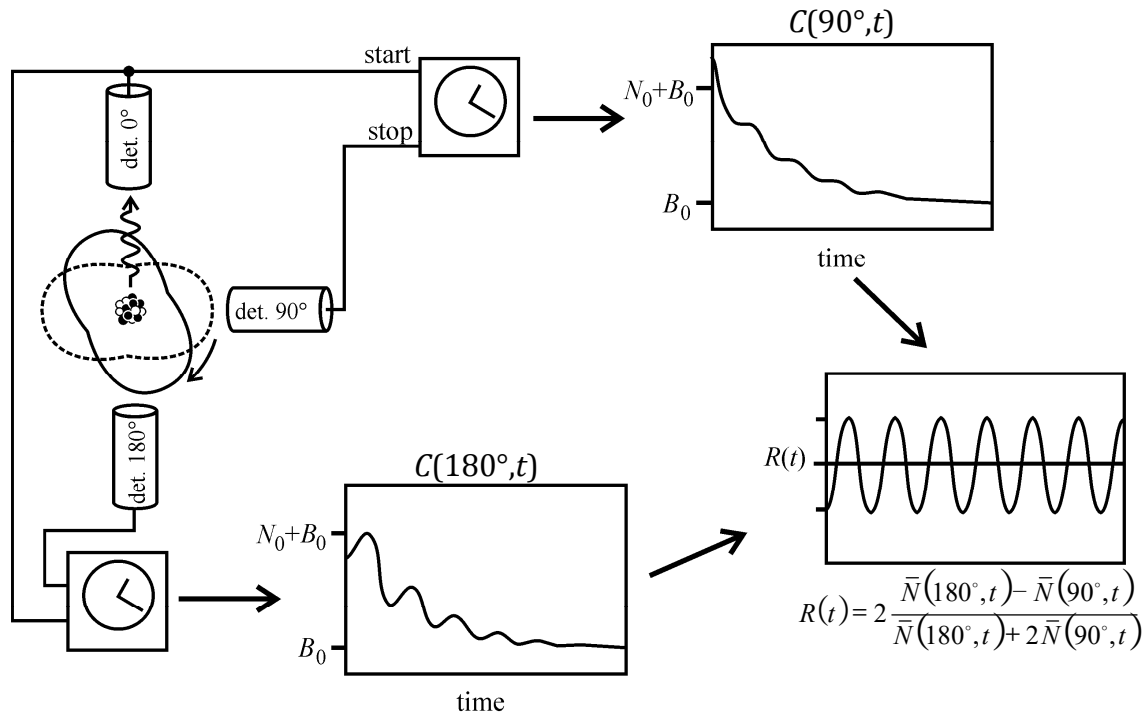

Fig. 8. Schematic of PAC data reduction.

is the number of true coincidences at angle θ_{ij} and time t, and $B_{ij}\left(\theta_{ij},t\right)$ is the number of accidental coincidences. True coincidences occur when both detected gamma rays came from the same nucleus, and $N_{ij}\left(\theta_{ij},t\right)$ is proportional to the angular correlation function $W\left(\theta_{ij},t\right)$. Accidental coincidences occur when detected gamma rays come from different nuclei; therefore, $B_{ij}\left(\theta_{ij},t\right)$ is independent of $W\left(\theta_{ij},t\right)$. The first step in the data reduction process usually involves subtraction of the background contributions from the total count rates, leaving $N_{ij}\left(\theta_{ij},t\right)$.

The number of true coincidences is given by $N_{ij}\left(\theta_{ij},t\right)=N_{0,ij}\exp\left(-t/\tau\right)W\left(\theta_{ij},t\right)$, where $N_{0,ij}$ is the number of counts at $t=0$ and τ is the mean lifetime of the intermediate nuclear state (the PAC level). The $N_{0,ij}$ depend in detail on the decay rate of the parent nucleus, on detector efficiencies, time resolution, and gamma absorption factors, the details of which can be found in ref. 58.

The modulations in coincidence count rate are contained entirely in $W\left(\theta_{ij},t\right)$. In order to isolate $W\left(\theta_{ij},t\right)$ from the factors $N_{0,ij}\exp\left(-t/\tau\right)$, one constructs a counting rate ratio $R(t)$, which can be thought of as a normalized difference of true coincidences between two different angles. One simultaneously can improve counting statistics and eliminate instrumental factors such as detector efficiencies by taking geometric averages of $N_{ij}\left(\theta_{ij},t\right)$ for detector-pairs that have equivalent angles θ_{ij}.

The most common spectrometer configuration has four detectors placed at 90° intervals in a plane. In this case, one conveniently can extract $W\left(\pi/2,t\right)$ and $W\left(\pi,t\right)$ using the conventional counting rate ratio defined by

$$R\left(t\right)=2\frac{\sqrt{N_{13}N_{24}}-\sqrt{N_{14}N_{23}}}{\sqrt{N_{13}N_{24}}+2\sqrt{N_{14}N_{23}}}, \tag{22}$$

where detector pairs 1-3 and 2-4 are 180° apart and detector pairs 1-4 and 2-3 are 90° apart. The $R(t)$ can be considered the PAC spectrum, and an example is shown in Fig. 9a. For a more general discussion of counting rate ratios, particularly those used in other experimental configurations, the reader is referred to the work of Arends *et al.* [58] and of Butz [21].

For a polycrystalline sample, it can be shown that Eq. 22 reduces to

$$R\left(t\right)=\sum_{\substack{k=2\\ \text{even}}}^{k_{max}}Q_{kk}A_{kk}\overline{G_{kk}}\left(t\right), \tag{23}$$

where Q_{kk} are attenuation factors that arise because of finite detector size [59]. It is common to report results in terms of effective anisotropy parameters, $A_{kk}^{\text{eff.}}\equiv Q_{kk}A_{kk}$.

For spectra obtained from polycrystalline samples, the second subscript on Q_{kk}, A_{kk}, and G_{kk} is redundant, and it usually is dropped. When using probes for which anisotropy terms of order higher than A_{22} can be neglected, the counting rate ratio is simply $R\left(t\right)=A_{2}^{\text{eff.}}\overline{G_{2}}\left(t\right)$. Some authors label

$R(t)$ plots in their papers as $A_2^{\text{eff.}} G_2(t)$. Other authors plot $-A_2^{\text{eff.}} G_2(t)$ when the anisotropy is negative (*e.g.*, in Fig. 9b). Other authors display spectra after dividing $R(t)$ by $A_2^{\text{eff.}}$ and label it $G_2(t)$ in order to provide a closer connection to the underlying physics of the hyperfine interactions (*e.g.*, in Fig. 9c). Often, authors display a Fourier transform of the perturbation spectrum to better illustrate the frequency multiplets – three frequencies in the case of spin-5/2 probes, (see Fig. 9d).

As can be seen in Fig. 9a-c, error bars increase with time between $\gamma-$ ray emissions. Estimated uncertainty in PAC experiments is based on the statistics of nuclear counting. For the channel corresponding to time interval t in the *i-j* histogram, $N_{ij}(\theta_{ij}, t)$, the uncertainty is estimated to be the standard deviation of a Gaussian distribution (assuming a large number of observed counts) with mean given by $N_{ij}(\theta_{ij}, t)$ so that the uncertainty is $\sqrt{N_{ij}(\theta_{ij}, t)}$. Hence, absolute uncertainties in collected data decrease with time as $\exp(-t/2\tau)$. The counting rate ratio of Eq. 22 is a normalized difference in counting rates at 180° and 90°, so the uncertainty in a data point of the counting rate ratio is effectively a relative counting uncertainty, $N/\sqrt{N}$, which is proportional to $\exp(t/2\tau)$. Thus, the error bars in the counting rate ratio increase in time.

Fitting. Following data reduction, PAC spectra are fitted to a theoretical expression of the perturbation function by varying parameters in the model function until a χ^2 goodness of fit parameter is minimized. Generally, an empirical form of the model perturbation function is used*:

$$\overline{G_{kk}}(t) = \sum_{j=1}^{N} f_j G_{kk,j}(t) \tag{24a}$$

with

$$G_{kk,j}(t) = \exp(-\lambda_j t)\left\{ s_{k0,j} + \sum_n s_{kn,j} \cos(\omega_{n,j} t) \exp\left[-\frac{1}{p}\left(\delta_j \omega_{n,j} t\right)^p\right]\right\}, \tag{24b}$$

for polycrystalline samples, which simultaneously takes into account multiple discrete static sites, inhomogeneous broadening**, and dynamic effects.

Best-fit values obtained from fits can provide information about defects in a material. Interaction frequencies $\omega_{n,j}$ often can be used to determine location(s) of probes, and what defects are near the probes by symmetry considerations, by comparison with results of DFT calculations, or by a combination of both. Variation in site fractions f_j can yield information about defect formation energies, defect association energies, and can help in identification of defect configurations by examining their dependence on temperature and sample composition. The degree of inhomogeneous broadening, δ_j, provides a qualitative measure of the concentration of randomly distributed defects in a material, and the dynamic damping parameter λ_j provides a measure of the rate at which defects jump near the probes. For non-polycrystalline samples, it is often possible to allow the s_{kn} parameters in Eq. 24b to vary as adjustable parameters, in which case Eq. 24 can be

---

* Conventionally, the model perturbation function is written without the bar: $G_{kk}(t)$. We have included the bar here to distinguish the measured perturbation function from the single-interaction perturbation functions in Eqs. 8, 9, 11.
** Again, there is some variation in Eq. 24b because of how the linewidth of the inhomogeneous broadening term is described.

used to analyze spectra obtained from single crystal samples provided that anisotropy terms of higher order than A_{22} can be neglected or included by further adjusting amplitudes.

Examples

This section examines how information about the properties and the processes related to defects can be obtained from parameters in Eq. 24 when fitting PAC spectra. Information obtained from interaction frequencies, site fractions, amplitudes, inhomogeneous broadening, and dynamic damping are considered separately. The discussion here is left largely in general terms with references provided to specific studies, many of which go into more detail regarding derivation of equations or methodology. Where possible, examples from multiple classes of materials are provided.

Interaction frequencies. The measured interaction frequencies provide information about the strength of the magnetic field present at the nucleus or of the distribution of charge surrounding the nucleus. Depending on the experiment, this can allow one to determine the location(s) of probes, how defects are arranged around probes, or charge states of defects. When different probe environments have distinct point symmetries, a simple consideration of symmetries of the observed EFGs can allow one to determine probe site occupation or arrangements of defects near the probes. Usually, more than just a symmetry consideration is needed, though. Examination of how site fractions change when varying experimental configurations such as sample composition, measurement temperature, annealing temperature, and sample orientation can help identify the origins of observed EFGs. In some cases, comparisons of strengths of measured QIs to predictions based on a simple point charge model or to QIs observed in analogous systems can allow identification of the sources of EFGs. In other cases, identifications can be made by comparison to predictions based on calculations using density functional theory.

The EFG underlying the QI is the quantity of interest in a study of materials properties, but the strength of the QI usually is reported (in terms of the quadrupole interaction frequency ω_Q or the quadrupole coupling frequency ν_Q) rather than the largest magnitude principle component of the EFG. This is because nuclear quadrupole moments, which are needed to calculate EFG components from interaction frequencies, generally are known with less precision than the measured frequencies. The EFG asymmetry parameter, on the other hand, does not depend on quadrupole moment, so that EFG asymmetries routinely are reported along with the QI strengths.

There have been a number of cases where site occupation could be determined by symmetries of EFGs alone. For example, the site occupation of indium in GdAl$_2$ was determined this way. The two primary EFGs observed had $\omega_Q = 0$ and $\omega_Q = 7.5$ Mrad/s with $\eta = 0$, which correspond to probes occupying the Gd site (with $4\bar{3}m$ site symmetry) and the Al site (with $\bar{3}m$ site symmetry) respectively [60]. As a second example, site occupation of indium in Zr$_2$Rh was based on observed EFG symmetries. The two EFGs observed had $\omega_Q = 13$ Mrad/s with $\eta = 0$ and $\omega_Q = 11$ Mrad/s and $\eta = 0.93$, which correspond to probes on the Rh-site (with $6m2$ site symmetry) and on the Zr site (with mm symmetry) respectively [61]. Other examples include indium site occupation in the HfAl$_2$ and ZrAl$_2$ Laves phases [62], and indium and hafnium in bixbyites [63, 64].

It is common for more than one lattice site in a compound to have the same site symmetry, in which case simple symmetry arguments cannot be used to determine the site occupation of a probe. In such cases, it is sometimes possible to determine site occupation by comparing signals to those obtained in isostructural compounds where site occupation of probes can be determined. Indium site occupation in Ga$_7$Pd$_3$ is a good example of this [65].

Ga$_7$Pd$_3$ and In$_7$Pt$_3$ have the Ge$_7$Ir$_3$ structure, in which there are two inequivalent Ge sites: Ge(1) with $\bar{4}m.2$ site symmetry and Ge(2) with $.3m$ site symmetry, both of which lead to axially symmetric EFGs. Two axially symmetric signals for indium in each system were observed:

ω_Q = 50.3 Mrad/s and ω_Q = 8.4 Mrad/s in In_7Pt_3 and ω_Q = 44.7 Mrad/s and ω_Q = 9.3 Mrad/s in Ga_7Pd_3. The ratio of Ge(1) sites to Ge(2) sites is 3:4 and the ratio of fraction of 50 Mrad/s to fraction of 8.4 Mrad/s signal in In_7Pt_3 was 3:4 ; therefore, one can attribute the higher frequency signal to Ge(1) sites and the lower frequency signal to Ge(2) sites. The ratio of high frequency to low frequency fractions in Ga_7Pd_3 was not 3:4 because indium is an impurity and does not distribute uniformly in the structure; however, one can attribute the 44.7 Mrad/s signal to indium on Ga(1) sites and the signal with 8.4 Mrad/s to indium on Ga(2) sites by analogy to observations in In_7Pt_3 [65].

Not all systems are as simple as Ga_7Pd_3, and identification of EFGs by analogy alone may not be possible because more EFGs are observed in the system-of-interest than in the isostructural reference compound. In such cases, it may be possible to determine origins of EFGs by using the point charge approximation. An example of this was identification of sites occupied by indium in Ni_2Al_3-structured compounds [66]. Another example involved picking out which of (several) observed EFGs corresponded to the defect-free EFGs in bixbyites [67], for which an empirical correction could be applied to allow comparison between different PAC probes and to compensate for shortcomings in the point charge model [30].

When results from analogous systems are not available, it may still be possible to identify occupation sites in complex compounds by comparison to predictions of EFGs calculated using density functional theory. A good example of this was the recent determination of indium site occupation in $(Hf/Zr)_3Al_2$ and $(Hf/Zr)_4Al_3$ [68].

Interaction frequencies provide a means of detecting defects near probes. When there is an attractive interaction between the PAC probe and defects, significant fractions of probes can be found in complexes with one or more defects. Measured interaction frequencies provide a "fingerprint" of sorts for each defect complex; however, the interaction frequencies alone typically do not allow one to identify the defect complex because multiple defect arrangements produce the same point symmetry at the PAC probe site.

In compounds where PAC probes sit at lattice sites with cubic point symmetry, detection of non-zero interaction frequencies indicates the presence of nearby point defects. It often is possible to obtain attributions for the origins of the EFGs causing the QIs by varying experimental conditions such as sample composition, measurement temperature, or oxygen partial pressure. For example, the farther a sample is from its stoichiometric composition, the more point defects will be present. Thus, defect complexes involving first one defect, then two defects, etc. would be observed as one increases the deviation from stoichiometry. This was used to identify indium, oxygen-vacancy complexes in CeO_2 [69] and indium, transition-metal-vacancy complexes in B2-structured compounds [26 and references therein]. As another example, monitoring the appearance and the disappearance of signals when varying oxygen partial pressure in CoO allowed attribution of different indium, cobalt-vacancy complexes [70].

As with site occupation, it is not always possible to identify which defect or defects induce an observed EFG by varying sample composition, measurement temperature and by using symmetry with simple arguments based on a point-charge approximation. In such cases, it may be possible to make a positive identification by comparing observed interaction frequencies to those predicted from calculations using density functional theory. For example, the charge states of acceptors and Te-vacancies in CdTe were determined by calculating EFGs induced by these defects when next to PAC probes using DFT calculations assuming neutral and ionized states for the defects and comparing the predictions with experiment [71].
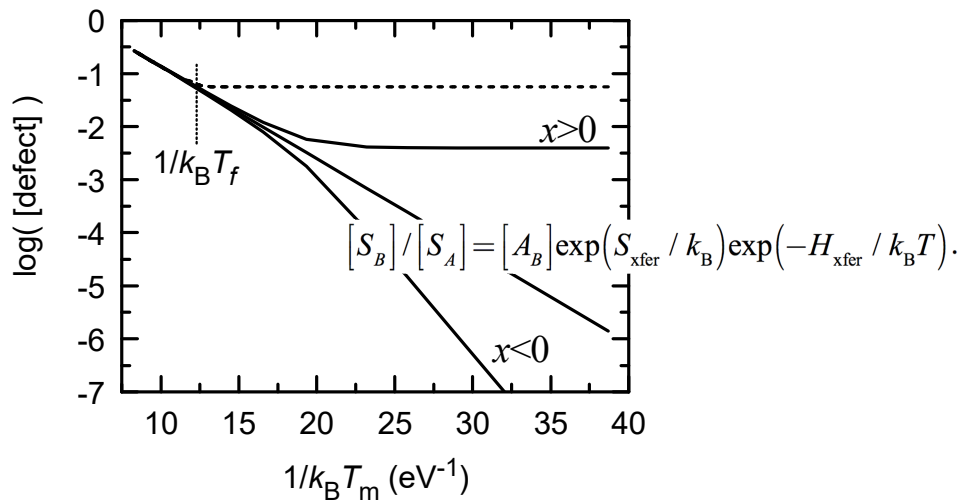
Site fractions. Qualitative examination of how site fractions vary with composition or temperature can aid in identifying origins of HFIs, as mentioned in the previous section. Moreover, quantitative analysis of these variations can yield information about defect thermodynamics. Depending on experimental conditions, it is possible to determine site occupation transfer energies, defect association energies, effective defect formation energies, and migration energies.

Composition and temperature dependences of defect concentrations in a material are coupled to changes in the free energy of the material accompanying the introduction of defects. Theoretical

expressions for equilibrium concentrations of defects can be obtained, for example, through minimization of a material's Gibbs free energy subject to structural and compositional constraints within the framework of the canonical ensemble. At the stoichiometric composition, the concentration of an intrinsic defect, $[\text{defect}]$, is given simply by $[\text{defect}] = \exp\left(S_F^{\text{eff.}} / k_B\right)\exp\left(-H_F^{\text{eff.}} / k_B T\right)$,

where $S_F^{\text{eff.}}$ is the effective formation entropy and $H_F^{\text{eff.}}$ is the effective formation enthalpy.

For non-stoichiometric compositions or in situations where extrinsic defects are non-negligible, [defect] depends in general on the deviation from stoichiometry and on concentrations of extrinsic defects. Fig. 10 illustrates the equilibrium concentration of an A antisite defect in a generic binary alloy $A_{1+x}B_{1-x}$ at three compositions (solid curves). At high enough temperature, [defect] is given by the stoichiometric value, and this is referred to below as the thermally activated regime. At low temperature for $x > 0$, in which case the A antisite is a constitutional defect, [defect] is independent of T to a good approximation. (For $x < 0$ at low T, [defect] also shows a thermally activated behavior with a different activation energy than $H_F^{\text{eff.}}$, but this is not considered further here.)

The dashed curve in Fig. 10 gives a schematic representation of the defect concentration actually measured in a material. At some temperature intrinsic defect concentrations are effectively "frozen in" when defects move too slow to allow equilibrium to be maintained. A rough estimate for the "freeze-in" temperature T_f can be made based on diffusivity. In an isotropic medium, the root-mean-square displacement r_{rms} over a time period τ is related to the diffusion coefficient by $D = \left\langle r_{\text{rms}}^2 \right\rangle / 6\tau$, and the diffusion coefficient is proportional to the defect jump rate: $w \propto w_0 \exp\left(-Q / k_B T\right)$, where w_0 is the attempt frequency and Q is the diffusion barrier in the potential-barrier model of diffusion. The estimate for T_f is found by solving for the temperature at which r_{rms} is equal to the average grain size in a sample. In Fig. 10, T_f was shown to lie in the "thermally activated" regime; however, there is nothing to prevent it from being in the non-thermally activated regime.

Site occupation of solutes in a compound is coupled to intrinsic defect concentrations.

Fig. 10. Equilibrium concentrations of A antisite defects in $A_{1+2x}B_{1-2x}$ with $H_F^{\text{eff.}} = 0.4$ eV and $S_F^{\text{eff.}} = 2\,k_B$ at $x = 0$ and $x = \pm 0.001$ (solid curves) as functions of measurement temperature T_m. There is a freeze-in temperature T_f below which the defect concentration will not be observed to change (dashed curve).

Examples of derivations of this in the framework of the canonical ensemble can be found, for example, in references 60 and 66. It can be explained using the Law of Mass Action in conjunction with a description of the transfer of a solute between two sites in terms of a quasi-chemical reaction. For example, solute transfer in the binary alloy $A_{1+x}B_{1-x}$ can be described by $S_A + A_B \rightarrow S_B + A_A$, where S stands for solute, the subscript indicates the site occupied, and the direction of the arrow indicates which direction corresponds a positive solute transfer enthalpy. The Law of Mass Action for this reaction gives

The ratio of site fractions of probes in sites B and A, f_B / f_A, is related to the concentrations by $f_B / f_A = N_B[S_B] / (N_A[S_A])$ where N_B is the number of B-sites per unit cell and N_A is the number of A sites. Thus, the ratio of site fractions will depend on composition through its dependence on $[A_B]$ and it will depend on temperature partly through its dependence on $[A_B]$ and partly because of the $\exp(-H_{xfer} / k_B T)$ factor. Usually, the magnitude of H_{xfer} is large and a solute resides on one "preferred" site throughout the temperature and composition measurement ranges. However, in some cases H_{xfer} is in the range for which changes in site fractions can be observed. Such changes in site fractions have been reported for Hf in LiNbO$_3$ and LiTaO$_3$ [72] and for In in GdAl$_2$ [60], Ni$_2$Al$_3$-structured compounds [66], ZrAl$_2$ and HfAl$_2$ [62], and Hf$_3$Al$_2$ [68]. Moreover, values of H_{xfer} were determined in the LiNbO$_3$, LiTaO$_3$, and GdAl$_2$ studies.

PAC is particularly sensitive to point defects in materials when there is an attractive interaction between the probe and defects so that probe-defect complexes form. The fraction of probes complexed with a defect is a function of defect concentration and temperature, and measurement of the site fraction as a function of temperature allows one to determine thermodynamic quantities such as the defect association energy. The connection between PAC site fractions and thermodynamic quantities is derived for a simple system in which probes are found either in a defect-free environment or as a probe-defect pair. The extension to larger clusters involving multiple defects is straightforward. Below, f_0 denotes the fraction of defect-free probes and f_p denotes the fraction of probes that are part of defect pairs.

The principle of detailed balance relates the probe fractions: $f_p r_d = f_0 r_t$ where r_t is the total rate at which the defect "traps," or jumps from a distant site to a near neighbor site of the probe, and r_d is the total detrap, or disassociation, rate. Under the usual assumptions of a potential-barrier model and of low defect concentrations, $r_d = z_d \nu_d \exp(S_D / k_B)\exp(-H_D / k_B T)$ and $r_t = z_t[\text{defect}]\nu_t \exp(S_M / k_B)\exp(-H_M / k_B T)$ where z_d is the number of detrapping pathways and z_t is the number of trap pathways. Note that $z_t = z_d z$ where z is the coordination number of the probe site. S_D and H_D are the entropy and the enthalpy of dissociation while S_M and H_M are for the barrier that the defect must overcome to jump from a distant site to a near neighbor site of the probe. The S_M and H_M may or may not be equivalent to comparable bulk quantities (that is, for defects far away from the PAC probe); however, it usually is assumed that any differences are negligible. Finally, ν_d and ν_t are the vibrational attempt frequencies.

The ratio of fractions is given by $f_p / f_0 = z[\text{defect}]\exp(S_A / k_B)\exp(-H_A / k_B T)$ where $H_A = H_M - H_D$ is the association enthalpy of the probe-defect pair and $S_A = S_M - S_D$ is the association entropy. A negative association enthalpy corresponds to an attraction between defects. Alternatively, the fraction ratio can be written in terms of binding enthalpy and entropy, $H_b = -H_A$ and $S_b = -S_A$ so that positive enthalpy corresponds to an attractive interaction.

Arguably, the most direct way of obtaining values for H_A and, when possible S_A, experimentally is by taking measurements at multiple temperatures, in which case f_p and f_0 correspond to the PAC site fractions. This method was used to study indium-transition metal

vacancy association in NiAl [73], FeAl [26], indium-cadmium vacancy association in CdTe [74], indium-samarium vacancy association in SmNi$_2$ [75], and a wide range of probe-solute pairs in metals [9].

In the non-thermally activated regime or for temperatures below T_f, [defect] is essentially independent of temperature so that the temperature-dependence of f_p / f_0 enters only through the $\exp(-H_A / k_B T)$ factor. Thus, a plot of $\ln(f_p / f_0)$ versus $1 / k_B T_m$, where T_m denotes the temperature of measurement, conveniently results in a straight line with slope $-H_A$ and intercept $\ln([\text{defect}]) - S_A/k_B$. More commonly, $\log(f_p / f_0)$ is plotted; this also results in a straight line, however the slope differs from H_A by a factor of $\ln(10)$ because of conversion between logarithm bases. Alternatively, enthalpies can be obtained directly from site fractions through nonlinear curve fitting. For the present example, $f_p + f_0 = 1$; therefore,

$$f_p = \left(1 + z^{-1}[\text{defect}]^{-1}\exp(-S_A / k_B)\exp(H_A / k_B T)\right)^{-1}.$$

In the thermally activated regime and temperatures above T_f, both the defect formation and the association factors contribute to the temperature dependence of f_p / f_0 so that a plot of $\ln(f_p / f_0)$ versus $1 / k_B T_m$ yields a slope proportional to $H_F^{\text{eff.}} + H_A$. Thus, one must have access to both the non-thermally and the thermally activated regimes in order to determine $H_F^{\text{eff.}}$ and H_A independently. Fig. 11 shows plots of $\log(f_p / f_0)$ versus $1 / k_B T_m$ and f_p versus T_m in both the thermally activated and non-thermally activated regimes. Note the temperature T_c indicated in the figure; it is the temperature where defect complex formation freezes, so that there is no variation in site fractions below this temperature. T_c is expected to be lower than the T_f of intrinsic defect formation as explained below.

The above expressions for r_d and r_t are rigorous when the defect is an interstitially diffusing defect or a vacancy, aside possibly from a correlation factor which generally is not included in derivations based on the principle of detailed balance. For substitutional defects diffusing via a simple vacancy mechanism, the above expressions are satisfactory as long as the vacancy jump rates are appreciably larger than the defect jump rates; otherwise correlation effects will be significant and will need to be included.

It is not always possible or practical to perform PAC measurements at elevated temperature, and many PAC studies of defect association, or rather disassociation, have been performed by collecting PAC spectra at room temperature following a sequence of anneals at elevated temperature, usually as an isochronal sequence. Here, two common types of experiments are described: (1) formation and dissociation of complexes formed between probes and intrinsic defects and (2) dissociation of complexes formed between probes and extrinsic defects.

In annealing studies of probe-intrinsic defect complexes, equilibrium concentrations of intrinsic defects initially are established at elevated temperature and then quenched into the sample by cooling to room temperature rapidly enough that equilibrium defect concentrations cannot be established. The cooling rate also is fast enough that defects do not have sufficient time to establish equilibrium concentrations of probe-defect complexes. So, initially there is a non-equilibrium distribution of defects and probe-defect complexes: an excess of intrinsic defects and a deficiency of probe-defect complexes. The first PAC measurement establishes a starting set of site fractions. Then, an anneal step, which allows distributions of defects to partly shift toward equilibrium, is performed. A subsequent PAC measurement will reveal a change in site fractions. The anneal – measurement sequence can be repeated as many times as needed.
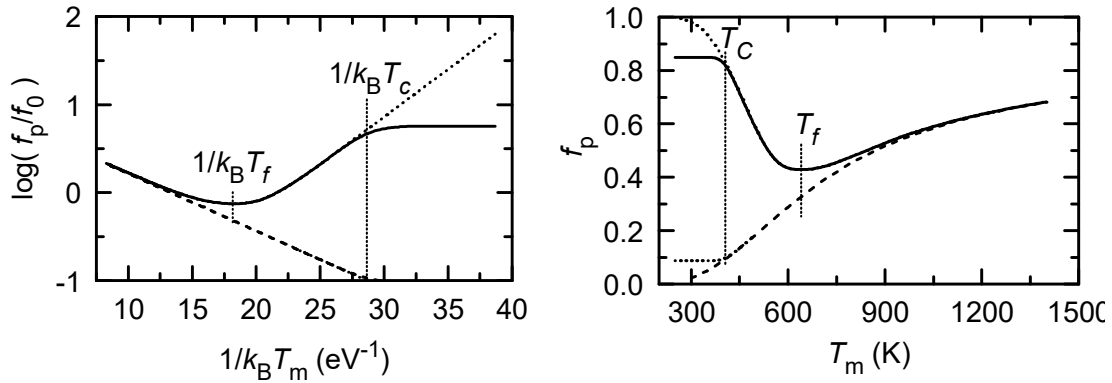
Fig. 11. Equilibrium association of probes with A antisite defects in $A_{1+2x}B_{1-2x}$ with $z = 8$, $H_A = -0.25$ eV, $S_A = 0$, and formation parameters in Fig. 10 as a function of measurement temperature T_m. Solid curves include effects caused by either defect formation freeze-in or by transition into the non-thermally activated regime whereas dashed curves indicate what would be observed if freeze-in did not occur. For the parameters in Fig. 10, the solid curves correspond to x = +0.001 with $1/k_B T_f$ above 20 eV^{-1}, but results would be similar for $x = 0$ with T_f as shown. Solid curves also include the effect of defect complex freeze-in at temperature T_c (see text), while dotted curves show what would be observed if this lower temperature freeze-in effect did not occur. As can be seen, there is a limited temperature range over which a pure Arrhenius behavior will be observed.

The rest of the discussion will consider again the simplified two-state case consisting only of defect-free probes and probes with one neighboring defect. Following the initial quench, $\left[\text{defect}\right] = \exp\left(S_F^{\text{eff.}} / k_B\right)\exp\left(-H_F^{\text{eff.}} / k_B T_Q\right)$ where T_Q is the quench temperature, which is equal to the T_f as determined by the rate of cooling. The site fraction ratio will be $f_p / f_0 = z\left[\text{defect}\right]\exp\left(S_A / k_B\right)\exp\left(-H_A / k_B T_c\right)$, where again T_c is the complex "freeze-in" temperature. For simplicity, it will be assumed that subsequent anneals take place below T_f so that [defect] does not change; however, f_p and f_0 will as the system evolves toward reaching an equilibrium number of probe-defect complexes.

In an anneal step, the sample is held at the target temperature for time t_A and the temperature is adjusted up or down rapidly enough so that to a good approximation, one can analyze changes in site fractions as occurring entirely at the anneal temperature T_A. At this temperature, the dissociation rate r_d and trap rate r_t are given by the same expressions as above, with $T = T_A$ and similar qualifiers for validity. In the equation for r_t, [defect] is the concentration of unpaired defects. As long as the concentration of probes is much smaller than [defect], so that the decrease in [defect] is negligible as pairing occurs, the trapping rate will be independent of time. This corresponds to the random telegraph process, which is a stationary Markov process, that is described by the Master equation(s) $df_p(t)/dt = -r_d f_p(t) + r_t f_0(t)$ and $df_0(t)/dt = -r_t f_0(t) + r_d f_p(t)$. The solution to these equations is

$$f_p(t_A) = \frac{r_t}{r_d + r_t}\left(1 - \exp\left[-\left(r_d + r_t\right)t_A\right]\right) + \exp\left[-\left(r_d + r_t\right)t_A\right]f_p(0) \tag{25}$$

where $f_p(0)$ is the fraction of probes with a near neighbor defect before the anneal, established by either the quench or a previous anneal step. Eq. 25 describes an exponential decay or growth from an initial fraction $f_p(0)$ to the equilibrium fraction $r_t / (r_d + r_t)$ with a lifetime given by $1 / (r_d + r_t)$. A simulation of f_p for a sequence of anneals is shown in Fig. 12.

Typically, an equation like Eq. 25 is not used to analyze site fractions in an anneal sequence. Rather, expressions derived assuming a single step, irreversible process for trapping (the left side of the peak in Fig. 12) or for disassociation (the right side of the peak in Fig. 12). For example, when trapping rates dominate over dissociation, the fraction of paired probes f_p can be found from the differential equation that describes association, $df_0 / dt = -r_t f_0$, and the normalization condition $f_p + f_0 = 1$ to get

$$f_p(t_A) = 1 - \exp(-r_t t_A)(1 - f_p(0)). \tag{26}$$

The solid curve in Fig. 12 is a plot of Eq. 26, and as can be seen, it agrees well with the data generated using Eq. 25, at least up until about the anneal temperature where dissociation becomes important, and it can provide a good estimate of migration barrier energy.

This type of analysis, or variations of it, have been used to study probe-defect formation and disassociation in semiconductors and metals. For example, this was used to analyze the formation and the dissociation of indium/cadmium-vacancy pairs in CdS [76]. A variation of this method, in which the excess vacancies were residuals of the radiation damage resulting from implantation of probes or from irradiation of samples rather than those frozen in after a quench from high temperature, was used to study association and disassociation of Pd-vacancy pairs in Si [77] and of In-vacancy complexes in fcc metals [4] and bcc metals [78, 79, 80, 81]. For the studies involving Si and the metals, vacancy concentrations were not constant so that Eq. 25 was not applicable, and analyses were based on an alternative equation (see ref. 4 for more information).
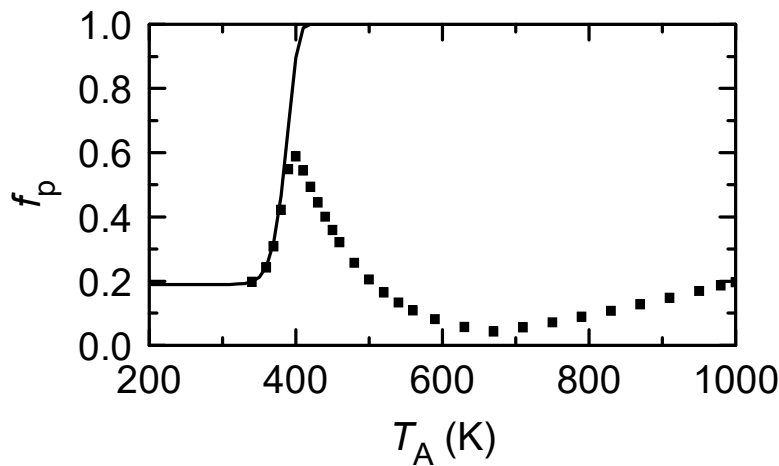

Fig. 12. Simulated study of probe-intrinsic defect association. Shown are measured site fractions of PAC probes that are paired with a defect following 10 minute anneals at the indicated temperatures (data points) for the physical parameters $z = 8$, $H_F^{eff.} = 0.6$ eV, $H_A = -0.35$ eV, $H_m = 1.0$ eV, $T_f = 670$ K, $T_Q = 800$ K, $T_c = 439$ K, and all entropies equal to zero. The curve is equation 26.
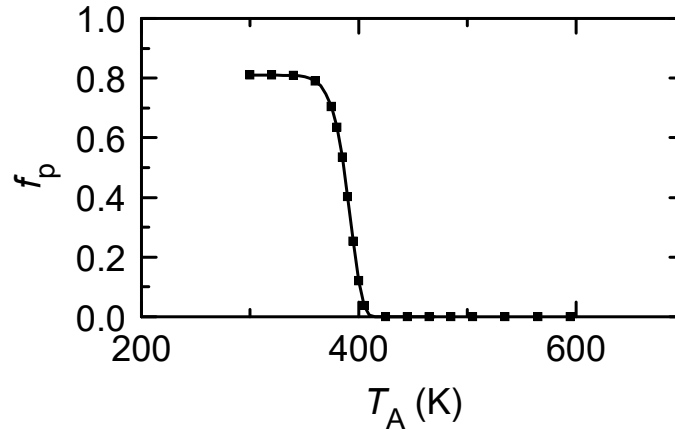
Fig. 13. Simulated study of probe-extrinsic defect association.
Shown are measured site fractions of PAC probes that are paired
with a defect following 10 minute anneals at the indicated
temperatures (data points) for the physical parameters $z = 8$,
$H_F^{\text{eff.}} = 3.6$ eV, $H_A = -0.9$ eV, $H_m = 0.4$ eV, and all entropies
equal to zero. The curve is equation 27.

In annealing studies of probe–extrinsic-defect dissociation, the first step is to establish an equilibrium, or near-equilibrium, number of probe-defect complexes. The lower the temperature at which this is done, the larger the fraction of probes will be found in complexes; however, the temperature needs to be above the complex formation freeze-in temperature. Anneal steps are then performed at higher temperatures. At each anneal temperature, the initial distribution of probe-defect complexes is not in equilibrium, and the anneal allows a partial shift towards equilibrium. As in the probe-intrinsic defect case, a PAC measurement after each anneal step reveals a change in site fractions.

Again, the simple two-state case consisting of defect-free probes and probes with one neighboring defect is considered. As long as anneals are done at temperatures below T_f, so that the concentration of extrinsic defects does not change, and as long the concentration of extrinsic defects is significantly larger than the concentration of probes, Eq. 25 is valid. A simulation of f_p for a sequence of anneals is shown in Fig. 13.

An equation derived assuming an irreversible single step process usually is used. So, under the assumption that retrapping rates are negligible, the relevant differential equation for dissociation is $df_p(t)/dt = -r_d f_p(t)$. The solution to this is $f_p(t_A)/f_p(0) = \exp(-r_d t_A)$, which can be rearranged to solve for an approximate value of H_D by taking $S_D = 0$:

$$H_D = k_B T_A \ln\left(z_d \nu_d t_A \ln\left(\frac{f_p(t_A)}{f_p(0)}\right)\right). \tag{27}$$

The solid curve in Fig. 13 is a plot of Eq. 27, and as can be seen it represents the data well. Most notably, dissociation of Cd-H complexes in III-V semiconductors and of In-acceptor complexes in Si and Ge were studied by monitoring changes in site fractions of probe-defect complexes with anneal temperature and calculating dissociation energies using Eq. 27, as summarized in the review by Deicher [11].

As a final note, Eq. 25 suggests a means of estimating T_c, the complex formation freeze-in temperature for *in situ* measurements. If activation enthalpies and entropies are known, an

approximate value for T_c is obtained by solving for the value of temperature such that $1/\left(r_d + r_t\right)$ equals the time needed to collect a PAC spectrum, which is typically 12 – 48 hours.

Amplitudes. The amplitudes in Eq. 24 deviate from their polycrystalline values when measurements are made on single crystal samples. The amplitudes depend in detail on orientation(s) of principal axes of EFGs and/or the directions of magnetic fields with respect to detector locations. Thus it is possible, within some limitations, to determine the orientation of HFI axes based on signal amplitudes. In crystals with high symmetry – especially those with cubic symmetry – a unique determination of EFG axis orientation will be possible only if the main principal axis is directed along one of the symmetry axes of the crystal because otherwise there is a large number of crystallographically equivalent orientations of the EFGs and the deviation in amplitudes from their polycrystalline values is diminished.

It is possible to take into account sample orientation with respect to detector placement, calculate perturbation functions, and fit spectra for single crystal samples rigorously – for example, by using the *DEPACK* software [82]. It also is possible to obtain information about orientations of hyperfine fields through a more qualitative examination of amplitude variation with sample orientation and detector configuration – illustrated nicely for the case of EFGs in cubic crystals in Fig. 3 of ref. 83.

It is reasonable to expect that determining the orientation of EFG principal axes would help in the identification of what types of defects are near a PAC probe or in determining the conformation of a defect complex. For example, in the zincblende structure, a substitutional probe without nearby defects would experience zero EFG. Nominally, a defect at the first neighbor site would lie in the <111> crystal direction whereas a defect in the second neighbor site would lie in the <110> crystal direction, each producing an axially symmetric EFG. Thus, measuring whether the axis of symmetry were in the <111> or the <110> direction would allow one to determine where the defect is located.

Lattice relaxations can reduce further the symmetry of the local crystal structure and the induced EFG, thereby affecting the orientation of the EFG principal axes as well as the values of the components (and the measured interaction frequencies). In samples with the zincblende structure, this would mean that the main principal axis of the EFG is along neither the <111> nor the <110> direction. For example, the main principal axes of EFGs experienced by substitutional indium probes with a second neighbor vacancy in II-VI compounds were not in the <110> direction as expected by symmetry considerations [13]. Lattice relaxation, and possibly an additional effect caused by a shift in electronic density near probes, was so strong in the cases of ZnSe and CdTe that the main principal axes were in the <111> direction [13].

Another good example of the undependability of EFG axis orientation can be seen in the EFGs experienced by Ta and Cd in TiO_2. The main principal axis of the EFG experienced by Hf is along the *c*-unit cell direction [35] whereas the main axis in the case of Cd was observed by PAC to be perpendicular to the *c*-axis [84]. In this case, the "undependability" originates from the inadequacy of symmetry arguments, which are based on a point charge picture, because contributions to the EFG by valence electrons dominate [35].

Observed orientations of EFGs are not always contrary to expectations based on symmetry. For example, orientations of most PAC probe/acceptor pairs in Si, Ge, and several III-V semiconductors are oriented along the <111> directions [11]; although, the orientation of the In-Te pair and of one of the In-Fe complexes in Si deviate [85, 86]. As another example, the indium-oxygen vacancy pair and the collinear arrangement of indium with two oxygen vacancies in CeO_2 also resulted in the main principal axis of the EFG along the <111> crystal direction [87].

Inhomogeneous broadening. Because inhomogeneous broadening is treated empirically, it currently is not possible to relate degree of inhomogeneous broadening to defect concentration or measures of other physical sources of broadening such as grain size. Nevertheless, the degree of inhomogeneous broadening does offer qualitative information about disorder in a sample that can be useful.

In studies that introduce PAC probes to samples via implantation techniques, radiation damage results in large concentrations of randomly distributed point defects in the region of the sample where the PAC probes are located. Observed PAC signals exhibit significant inhomogeneous broadening in such cases. Depending on the material and on the probe, the observed PAC signals could be broadened signals that arise from probes without defects in the first or second neighbor shell, as was the case for indium implanted in ZnO [88], in GaP [89], and in Nb [90], or that arise from probes with defects in the first or second neighbor shell, as was the case for Pd in Nb [90].

Following implantation, one expects to be able to reduce the number of defects by annealing at a temperature high enough for defects to be sufficiently mobile to recombine, at least partially. Indeed, isochronal anneal sequences with PAC measurements in between anneal steps typically show decreases in the degree of inhomogeneous broadening that is correlated to the reduction of defects. This is illustrated nicely in the two recent papers on indium implanted in ZnO [88] and GaP [89].

The sensitivity of the PAC signal linewidth to lattice defects suggests that PAC could be used as an atomic-scale probe of crystalline structure in highly disordered material. However, it has been shown that care must be taken when drawing conclusions regarding disorder throughout a sample based on the PAC signal. For example, two types of environments of Hf probes were observed in metamict zircon: (1) a moderately defective crystalline environment and (2) a nearly, if not completely, amorphous environment [91]. Annealing resulted in an increase of the site fraction of probes found in the crystalline environment and a decrease of the site fraction of probes found in the amorphous environment; however, the fraction of probes in the crystalline environment was smaller than what was expected based on the volume fractions of the two environments determined using conventional X-ray diffraction (XRD). The discrepancy was attributed to the difference in length scales probed by PAC and by XRD [91].

In PAC studies of Cu-Hf alloys, a significant site fraction of probes were in a crystalline state resembling Cu_3Hf_2 [92] even though the sample composition was $Cu_{57}Hf_{43}$ and XRD indicated that the sample was amorphous [93]. This discrepancy may again be attributable to the difference in length scales probed by the two methods. As pointed out by Kanazawa, the Cu-Hf result suggests that PAC could provide a better measure of amorphization quality than XRD [93], which certainly looks to be the case in Cu-Hf. However, the zircon results show that PAC alone is not reliable for such a characterization in general. Hence, it looks like a combination of PAC and techniques that are sensitive to long-range order, such as XRD, is required for complete characterization.

Dynamic damping. The most commonly observed source of dynamic damping occurs when the jump of a defect near the probe results in a change of the HFI at the probe or when a jump of the probe itself results in a change in the HFI. For simplicity, we shall assume that there is a one-to-one correspondence between a defect jump and a change in the HFI so that the rate at which the HFI changes is equal to the jump of a defect.

In the usual potential-barrier model of atomic jumps, the jump rate w of a point defect is given by $w = cw_0 \exp\left(S_m / k_B\right)\exp\left(-H_m / k_B T\right)$ where w_0 is the attempt frequency, S_m is the migration entropy, H_m is the migration enthalpy, or migration barrier, and c is a factor that describes the availability of neighboring sites to which the defect can jump. For diffusion of a tracer in a metallic system via a simple vacancy diffusion mechanism, the availability is given by $c = Z[V]$ where Z is the number of near neighbors on the solute's sublattice and $[V]$ is the concentration of vacancies on that sublattice.

When using the empirical form of Eq. 24b, the damping factor λ is proportional to the HFI fluctuation frequency, and in turn to the underlying defect jump rate, in the slow fluctuation regime, and λ is inversely proportional to the fluctuation frequency in the rapid fluctuation regime.   Thus a plot of $\ln(\lambda)$ versus $1/k_B T$ in the slow regime would yield a straight line, the slope of which is equal to $-H_m$ and a plot of $\ln(\lambda)$ versus $1/k_B T$ in the rapid regime would yield a slope equal to $+H_m$.

A number of studies have utilized an empirical analysis to study defect jump rates near probes. These include the observation of H jumps near Hf in yttrium, hafnium, and dysprosium hydrides [94, 95, 96], of H jumps near Cd in Si [97] and HfV_2H_x [98], of Cu jumps near Cd in Si [99], of rare-earth (R) vacancy jumps near Cd in $R_{1-x}Ni_2$ [75], and of oxygen vacancies in $R_2M_2O_7$ (R = Nd, Sm, Eu, and Gd; M = Zr and Hf) pyrochlores [100] and in CeO_2 [69]. Examples of how such an empirical analysis has been used to study the motion of the PAC probe itself include studies of Cd jump rates in –Mn [101], Pd_3Ga_7 [102], Pt_3Ga_7 [103], $Al_{11}R_3$ (R = La, Ce, Pr) [104], and $LaSn_3$ [105].

An alternative way to determine defect jump rates from PAC spectra is to fit spectra with test functions generated from numerical solutions to an appropriate stochastic model. This method was used to determine Cd jump rates in RIn_3 (R = La, Ce, Pr, Er, Nd, and Y) [106, 107] and RGa_3 (R = Dy, Er, Lu) [108].

Another important physical origin of fluctuating HFIs arises from a fluctuation in charge states of defect complexes involving the PAC probe. This was reported to occur for Cd-H and Cd-D (D = P, As, Sb) complexes in Si [109]. In this case, it was possible to find an analytical solution to Eq. 20 [110], which is a rare occurrence. Charge fluctuations in these studies were in the rapid fluctuation regime, and it was possible to obtain fluctuation rates and relative populations of charge states.

For very large fluctuation rates, damping factors become too small to measure and the perturbation function is equal to simply $G_{kk,\text{M.A.}}(t)$. It is possible to express the time average of accessible HFIs in terms of relative fractions of probes in the accessible HFIs so that one can determine relative populations of defect configurations. For example, this was the method employed in the original analysis of Cd-H charge states in Si [111]. It also was applicable to the case of rapid trapping and detrapping of oxygen vacancies to Cd probes in tetragonal ZrO_2 so that it was possible to determine equilibrium occupation probabilities of vacancies in sites next to probes as a function of temperature, which allowed determination of the cadmium/oxygen vacancy binding energy [112].

Summary

An introduction to perturbed angular correlation spectroscopy with an emphasis on its application in the study of point defects and diffusion was presented. This included explanations of the theoretical underpinnings of the technique, of the origin of the quadrupole interaction in solids, of probe selection and spectrometer configuration, and of a tutorial on how different physical parameters of interest to the study of defects and diffusion can be obtained from the analysis of PAC spectra. Brief explanations of a number of example studies were provided, arranged based on the analysis methods used. These are summarized in Table 2, arranged by the type of material and the general physical phenomenon considered.

Acknowledgements

Table 2: Summary of cited PAC studies. Below, R is short for rare-earth element and M is short for transition metal.

	Metallic compounds	Semiconductors	Ceramics
Solute site occupation	• In in $GdAl_2$ [60] • In in Zr_2Rh [61] • In in $HfAl_2$ & $ZrAl_2$ [62] • In in Pd_3Ga_7 [65] • In in Ni_2Al_3 & related [66] • In in $(Hf/Zr)_3Al_2$ & $(Hf/Zr)_4Al_3$ [68]		• In & Hf in bixbyites [63, 64, 67] • Hf in $LiNbO_3$ & $LiTaO_3$ [72]
Probe:defect complex configurations	• In:V_M in B_2 compounds [26]	• Cd:acceptor and Cd:V_{Te} charge states in CdTe [71] • Cd:vacancy in II-VI compounds [13] • Cd:acceptor in III-Vs, Si, and Ge [11, 85, 86]	• In:V_O in CeO_2 [69] • In:V_O in CoO [70] • In:V_O in CeO_2 [87]
Probe:defect interactions	• In:V_{Ni} in NiAl [73] • In:V_{Fe} in FeAl [26] • In:V_{Sm} in $SmNi_2$ [75] • Probe:solute pairs in metals [4] • In:vacancy pairs in metals [9, 78—81]	• In:V_{Cd} in CdTe [74] • In:V_{Cd} in CdS [76] • Pd:V_{Si} in Si [77] • Cd:H in III-V compounds [11] • Cd:acceptors in Si & Ge [11]	• Cd:V_O in ZrO_2 [112]
Atomic jumps	• H near Hf in Y [94], Hf [95], & $DyH_{2\pm\delta}$ [96] • H near Cd in HfV_2H_x [98] • V_R near Cd in $R_{1-x}Ni_2$ [75] • Cd in β-Mn [101] • Cd in Pd_3Ga_7 [102] & Pt_3Ga_7 [103] • Cd in $Al_{11}R_3$ [104] • Cd in $LaSn_3$ [105], RIn_3 [106, 107], & RGa_3 [108]	• H near Cd in Si[97] • Cu near Cd in Si[99]	• V_O near Ta in $R_2M_2O_7$ [100] • V_O near Cd in CeO_2 [69]
Charge fluctuations		• Cd:H & other Cd:dopant pairs in Si [109—111]	
Highly disordered materials	Nb [90] Cu-Hf [92, 93]	• ZnO [88] • GaP [89]	$ZrSiO_4$ [91]

References

1. H. Haas and D. A. Shirley: Journal of Chemical Physics Vol. 58 (1973), p. 3339.

2. B. I. Deutch: Atomic Energy Review Vol. 12 (1974), p. 605.

3. H. H. Rinneberg: Atomic Energy Review Vol. 17 (1979), p. 477.

4. Frits Pleiter and Christoph Hohenemser: Phys. Rev. B Vol. 25 (1982), p. 106.

5. Ekkehard Recknagel, Guenter Schatz, and Thomas Wichert: Topics in Current Physics Vol. 31, (1983), p. 133.

6. R. Vianden: Hyperfine Interact. Vol. 35 (1987), p. 1079.

7. A. Lerf and T. Butz: Hyperfine Interact. Vol. 36 (1987), p. 275.

8. R. Vianden: NATO ASI Series, Series E: Applied Sciences Vol. 144 (1988), p. 239.

9. R. Królas: Hyperfine Interact. Vol. 60 (1990), p. 581.

10. Gary S. Collins, Steven L. Shropshire, and Jiawen Fan: Hyperfine Interact. Vol. 62 (1990), p. 1.

11. M. Deicher: Nuclear Instruments and Methods in Physics Research Vol. B63 (1992), p. 189.

12. M. Deicher: Hyperfine Interact. Vol. 79 (1993), p. 681.

13. Thomas Wichert: Materials Research Society Symposium Proceedings Vol. 378 (1995), p. 237.

14. Thomas Wichert: Semiconductors and Semimetals Vol. 51B (1999), p. 297.

15. Michael Uhrmacher: Physica B Vol. 389 (2007), p. 58.

16. Rakesh Dogra, A. P. Byrne, and M. C. Ridgway: Journal of Electronic Materials Vol. 38 (2009), p. 623.

17. G. Schatz and A. Weidinger: Nuclear Condensed Matter Physics: Nuclear Methods and Applications (John Wiley, New York, 1996).

18. R. M. Steffen and K. Alder, in: *The Electromagnetic Interaction in Nuclear Spectroscopy*, edited by W. D. Hamilton, North-Holland Publishing Company, Amsterdam (1965).

19. H Frauenfelder and R. M. Steffen, in: *Alpha-, Beta- and Gamma-Ray Spectroscopy*, edited by K. Siegbahn, North-Holland Publishing Company, Amsterdam (1965).

20. Artur Wilson Carbonari, José Mestnik-Filho, and Rajendra Narain Saxena: current volume.

21. T. Butz: Hyperfine Interact. Vol. 52 (1989), p. 189.

22. L. A. Mendoza-Zélis, A. G. Bibiloni, M. C. Caracoche, A. R. Lopéz-García, J. A. Martínez, R. C. Mercader, and A. F. Pasquevich: Hyperfine Interact. Vol. 3 (1977), p. 315.

23. D. Wegner: Hyperfine Interact. Vol. 23 (1985), p. 179. Note that the first factor in parentheses in Eq. 5b is incorrect and should be replaced by $(1-\eta^2)$.

24. E. Matthias, W. Schneider, and R. M. Steffen: Phys. Rev. Vol. 125 (1962), p. 261.

25. T. M. Rearick, G. L. Catchen, and J. M. Adams: Phys. Rev. B Vol. 48 (1993), p. 224.

26. G. S. Collins, L. S. J. Peng, and M. O. Zacate: Defect and Diffusion Forum Vol. 213-215 (2003), p. 107.

27. R. M. Sternheimer: Phys. Rev. Vol. 130 (1963), p. 1423.

28. F. D. Feiock and W. R. Johnson: Phys. Rev. Vol. 187 (1969), p. 39.

29. R. N. Attili, M. Uhrmacher, K. P. Lieb, L. Ziegeler, M. Mekata, and E. Schwarzmann: Phys. Rev. B Vol. 53 (1996), p. 600.

30. M. Rentería, C. P. Massolo, and A. G. Bibiloni: Mod. Phys. Lett. B Vol. 6 (1992), p. 1818.

31. W. W. Simmons and C. P. Slichter: Phys. Rev. B Vol. 121 (1961), p. 1580.

32. R. S. Raghavan, E. N. Kaufmann, and P. Raghavan: Phys. Rev. Lett. Vol. 34 (1975), p. 1280.

33. P. Raghavan, E. N. Kaufmann, R. S. Raghavan, E. J. Ansaldo, and R. A. Naumann: Phys. Rev. B Vol. 13 (1976), p. 2835.

34. D. Torumba, K. Parlinski, M. Rots, and S. Cottenier: Phys. Rev. B Vol. 74 (2006), p. 144304; and references therein.

35. G. N. Darriba, L. A. Errico, P. D. Eversheim, G. Fabricius, and M. Rentería: Phys. Rev. B Vol. 79 (2009), p. 115213.

36. A. M. Stoneham: Reviews of Modern Physics Vol. 41 (1969), p. 82.

37. A. J. Pustowka, B. D. Sawicka, and J. A. Sawicki: Physica Status Solidi B: Basic Research Vol. 57 (1973), p. 783.

38. M. Forker: Nuclear Instruments and Methods Vol. 106 (1973), p. 121.

39. C. Budtz-Jørgensen and K. B. Nielsen: Hyperfine Interact. Vol. 1 (1975), p. 81.

40. H. J. Stöckmann: Journal of Magnetic Resonance Vol. 44 (1981), p. 145.

41. P. J. Bryant and S. Hacobian: Journal of Molecular Structure Vol. 83 (1982), p. 311.

42. G. Le Caër and R. A. Brand: Journal of Physics: Condensed Matter Vol. 10 (1998), p. 10715; and references therein.

43. A. P. Ayala and A. López-García: Hyperfine Interact. Vol. 120/121 (1999), p. 163.

44. T. Butz: Physica Scripta Vol. 78 (2008), p. 015801.

45. M. A. Alves, N. Mommer, J. A. Gardner, and W. E. Evenson: Hyperfine Interact. Vol. 136/136 (2002), p. 573.

46. R. E. Alonso and A. López-García: Zeitschrift für Naturforschung, A: Physical Sciences Vol. 55 (2000), p. 261.

47. H. Winkler and E. Gerdau: *Z. Phys.* Vol. 262 (1973), p. 363.

48. M. O. Zacate and W. E. Evenson: Computer Physics Communications (accepted 2010).

49. W. E. Evenson, H. Guan, J. Lu, and J. A. Gardner: Hyperfine Interact. Vol. (C)1 (1996), p. 392.

50. Hui Guan, Models of Perturbed Angular Correlations in Fluctuating Electric Field Gradients, PhD Dissertation, Brigham Young University, April 1994.

51. Jun Lu, Stochastic Models of Perturbed Angular Correlation Due to Diffusion of Defects in Materials, PhD Dissertation, Brigham Young University, June, 1995.

52. A. Baudry and P. Boyer: Hyperfine Interact. Vol. 35 (1987), p. 803.

53. M. Forker, W. Herz, and D. Simon: Nuclear Instruments and Methods in Physics Research A Vol. 337, p. 534.

54. M. Haaks, R. Valentini, and R. Vianden: Phys. Stat. Sol. (c) Vol. 4 (2007), p. 4036.

55. A. Bartos, K. Schemmerling, Th. Wenzel, and M. Uhrmacher: Nuclear Instruments and Methods in Physics Research Section A: Accelerators, Spectrometers, Detectors and Associated Equipment Vol. 330 (1993), p. 132.

56. C. Herden, J. Röder, J. A. Gardner, and K. D. Becker: Nuclear Instruments and Methods in Physics Research A Vol. 594 (2008), p. 155.

57. Matthias Nagl, Ulrich Vetter, Michael Uhrmacher, and Hans Hofsäss: Review of Scientific Instruments Vol. 81 (2010), p. 073501.

58. A. R. Arends, C. Hohenemser, F. Pleiter, H. De Waard, L. Chow, and R. M. Suter: Hyperfine Interact. Vol. 8 (1980), p. 191.

59. For example, H. Frauenfelder, R. M. Steffen, S. R. De Groot, H. A. Tolhoek, and W. J. Huiskamp, in: *Alpha-, Beta-, and Gamma-Ray Spectroscopy*, vol. 2, edited by Kai Siegbahn, North-Holland Publishing Company, Amsterdam (1965).

60. M. O. Zacate and G. S. Collins: Phys. Rev. B Vol. 69 (2004), p. 174202.

61. P. Wodniecki, A. Kulińska, B. Wodniecka, and M. Uhrmacher: Journal of Alloys and Compounds Vol. 448 (2008), p. 69.

62. P. Wodniecki, B. Wodniecka, A. Kulińska, M. Uhrmacher, and K. P. Lieb: Journal of Alloys and Compounds Vol. 335 (2002), p. 20.

63. J. Shitu, D. Wiarda, T. Wenzel, M. Uhrmacher, K. P. Lieb, S. Bedi, and A. Bartos: Phys. Rev. B Vol. 46 (1992), p. 7987; and references therein.

64. Leonardo A. Errico, Mario Rentería, Anibal G. Bibiloni, and Kristian Freitag: Physica B: Condensed Matter Vol. 389 (2007), p. 124; and references therein.

65. E. R. Nieuwenhuis, M. O. Zacate, and G. S. Collins: Defect and Diffusion Forum Vol. 264 (2007), p. 27.

66. M. O. Zacate and G. S. Collins: Phys. Rev. B Vol. 70 (2004), p. 024202.

67. For example, Mario Rentería, Kristian Freitag, and Leonardo A. Errico: Hyperfine Interact. Vol. 120/121 (1999), p. 449.

68. L. A. Errico, H. M. Petrilli, L. A. Terrazos, A. Kulińska, P. Wodniecki, K. P. Lieb, M. Uhrmacher, J. Belosevic-Cavor, and V. Koteski: J. Phys.: Condens. Matter Vol. 22 (2010), p. 215501.

69. R. Wang, J. A. Gardner, W. E. Evenson, and J. A. Sommers: Phys. Rev. B Vol. 47 (1993), p. 638.

70. Th. Wenzel, M. Uhrmacher, and K. P. Lieb: Philosophical Magazine A Vol. 72 (1995), p. 1099.

71. Thomas Wichert and Stephan Lany: Hyperfine Interact. Vol. 136/137 (2001), p. 453; and references therein.

72. Gary L. Catchen, James M. Adams, and Todd M. Rearick: Phys. Rev. B Vol. 46 (1992), p. 2743.

73. M. O. Zacate and G. S. Collins: Defect and Diffusion Forum Vol. 194-199 (2001), p. 383.

74. J. W. Griffith, R. Lundquist, R. Platzer, John A. Gardner, G. Karczewski, and J. K. Furdyna: Materials Science Forum Vol. 143-147 (1994), p. 405.

75. M. Forker, P. de La Presa, S. Müller, A. Lindbaum, and E. Gratz: Phys. Rev. B Vol. 70 (2004), p. 014302.

76. Thomas Wichert, Thomas Krings, and Herbert Wolf: Physica B Vol. 185 (1993), p. 297.

77. D. A. Brett, R. Dogra, A. P. Byrne, J. Mestnik-Filho, and M. C. Ridgway: Phys. Rev. B Vol. 72 (2005), p. 193202.

78. A. Weidinger, R. Wessner, E. Recknagel, and Th. Wichert: Nucl. Inst. Meth. Vol. 182/183 (1981), p. 509.

79. R. Sielemann, H. Metzner, R. Butt, S. Klaumuenzer, H. Haas, and G. Vogl: Phys. Rev. B Vol. 25 (1982), p. 5555.

80. R. Sielemann, H. Metzner, E. Hunger, and S. Klaumuenzer: Phys. Lett. Vol. 117A (1986), p. 87.

81. G. J. van der Kolk, K. Post, A. van Veen, F. Pleiter, and J. Th. M. de Hosson: Radiation Effects Vol. 84, (1985), p. 131.

82. B. Lindgren: Hyperfine Interact. Vol. C1 (1996), p. 613.

83. M. Deicher and W. Pfeiffer: Materials Science Forum Vol. 148-149 (1994), p. 481.

84. L. A. Errico, G. Fabricius, M. Rentería, P. de la Presa, and M. Forker: Phys. Rev. Lett. Vol. 89 (2002), p. 055503.

85. G. Tessema and R. Vianden: Applied Physics A Vol. 81 (2005), p. 1471.

86. U. Reislöhner and W. Witthuhn: Mater. Science Forum Vol. 65/66 (1991), p. 281.

87. Matthew O. Zacate, A microscopic Study of the Interaction Between Aliovalent Dopants and Native Defects in Group IV Oxides: Indium and Cadmium in Ceria and Zirconia, PhD Thesis, Oregon State University, June 1997.

88. R. Dogra, A. P. Byrne, M. C. Ridgway: Optical Materials Vol. 31 (2009), p. 1443.

89. R. Dogra, Z. S. Hussain, and A. K. Sharma: Materials Characterization Vol. 58 (2007), p. 652.

90. R. Sielemann, H. Metzner, R. Butt, S. Klaumünzer, H. Haas, and G. Vogl,: Phys. Rev. B Vol. 25 (1982), p. 5555.

91. H. Jaeger, M. P. Rambo, and R. E. Klueg: Hyperfine Interact. Vol. 136/137 (2001), p. 515.

92. I. Kanazawa, T. Oguchi, T. Ohata, K. Tokumitsu, Y. Sakurai, S. Nanao, and T. Iwashita: Phys. Rev. B Vol. 47 (1993), p. 7732.

93. I. Kanazawa: Phys. Rev. B Vol. 50 (1994), p. 9635.

94. M. Forker, U. Hütten and M. Müller: J. Phys.: Condens. Matter Vol. 12 (200), p. 7117; and references therein.

95. M. Forker, L. Freise, D. Simon, H. Saitovitch, and P. R. J. Silva: Hyperfine Interact. Vol. 35 (1987), p. 829; references therein.

96. M. Forker and U. Hütten: Phys. Rev. B Vol. 53 (1996), p. 5396.

97. M. Gebhard, B. Vogt, and W. Witthuhn: Phys. Rev. Lett. Vol. 67 (1991), p. 847.

98. M. Forker, W. Herz, D. Simon, and S. C. Bedi: Phys. Rev. B Vol. 51 (1995), p. 15994.

99. R. Keller, M. Deicher, R. Magerle, W. Pfeiffer, H. Skudlik, and Th. Wichert: Nuclear Instruments & Methods in Physics Research Vol. B63 (1992), p. 202.

100. G. L. Catchen and T. M. Rearick: Phys. Rev. B Vol. 52 (1995), p. 9890.

101. M. O. Zacate and G. S. Collins: Defect and Diffusion Forum Vol. 237-240 (2005), p. 396.

102. E. R. Nieuwenhuis, M. O. Zacate, and G. S. Collins: Defect and Diffusion Forum Vol. 264 (2007), p. 27.

103. Farida Selim, John P. Bevington, and Gary S. Collins: Hyperfine Interact. Vol. 178 (2007), p. 333.

104. Stephanie Lage and Gary S. Collins: Defect and Diffusion Forum Vol. 289-292 (2009), p. 755.

105. G. S. Collins, A. Favrot, L. Kang, E. R. Nieuwenhuis, D. Solodovnikov, J. Wang, and M. O. Zacate: Hyperfine Interact. Vol. 159 (2005), p. 1.

106. M. O. Zacate, A. Favrot, and G. S. Collins: Phys. Rev. Lett. Vol. 92 (2004), p. 225901; Erratum, Phys. Rev. Lett. Vol. 93 (2004), p. 49903.

107. G. S. Collins, A. Favrot, L. Kang, D. Solodovnikov, and M. O. Zacate: Defect and Diffusion Forum Vol. 237-240 (2005), p. 195.

108. Xia Jiang, Matthew O. Zacate, and Gary S. Collins: Defect and Diffusion Forum Vol. 289-292 (2009), p. 725.

109. W. Witthuhn: Nuclear Instruments and Methods in Physics Research Vol. B63 (1992), p. 209.

110. Norbert Achtziger and Wolfgang Witthuhn: Phys. Rev. B Vol. 47 (1993), p. 6990.

111. A. Baurichter, S. Deubler, D. Forkel, M. Gebhard, H. Wolf, W. Witthuhn, and M. Uhrmacher: Materials Science and Engineering Vol. B4 (1989): p. 281.

112. Niels Mommer, Theresa Lee, John A. Gardner, and William E. Evenson: Phys. Rev. B Vol. 61 (2000), p. 162.